

Politecnico di Torino

Politecnico di Torino

Master's Degree in Energy and Nuclear Engineering

A.A. 2025/2026

Graduation Session September 2026

Modeling and Techno-Economic Assessment of a Small-Scale Organic Rankine Cycle with Parabolic Dish Collectors

Supervisor:
Prof. Davide Papurello

Candidate:
Cosimo Guarino

Abstract

The transition towards low-carbon energy systems has increased interest in technologies capable of converting medium-temperature renewable heat into both electrical and thermal energy. In this context, small-scale Organic Rankine Cycles coupled with solar concentrators represent a possible solution for decentralized cogeneration, although their performance depends on the working fluid, cycle configuration and solar-field design.

This thesis investigates a small-scale Organic Rankine Cycle coupled with parabolic dish collectors and designed for the combined production of electricity and useful heat. The system was modeled under steady-state conditions in Aspen Plus using the Peng–Robinson equation of state. The thermal energy collected by the solar field is transferred to the ORC evaporator through a pressurized Dowtherm-A circuit.

Three working fluids were considered: MDM, toluene and D4. The turbine, condenser, pump and evaporator were first modeled separately, and sensitivity analyses were performed to determine suitable operating conditions. The comparison was carried out by imposing the same nominal turbine power output of 10 kW for all fluids. The condenser was designed to heat water from 60 °C to approximately 85 °C, allowing useful heat recovery for cogeneration purposes.

The component models were then integrated into a base and a regenerative configuration, the latter based on two expansion stages and an intermediate extraction of the working fluid. For all fluids, regeneration reduced the evaporator thermal demand and the number of collectors required, but also decreased the total turbine power output and the useful heat recovered at the condenser.

The annual operating time was estimated from representative seasonal temperature profiles at the collector focus, while the solar field was sized according to the evaporator thermal demand. Toluene provided the most favorable balance between cycle efficiency, thermal requirements and solar-field size.

Finally, the investment costs of the base and regenerative toluene configurations were estimated through the adopted capital-cost methodology. Their economic performance was compared through the Net Present Value over the assumed plant lifetime. Under the considered assumptions, the base configuration achieved the highest NPV despite its larger initial investment.

Table of Contents

List of Tables IV

List of Figures VI

Acronyms IX

1 Solar Energy: Concentrated Solar Power Systems 1
- 1.1 General overview . . . 1
- 1.2 Classification of CSP systems . . . 2
  - 1.2.1 Linear Fresnel Reflector Systems . . . 3
  - 1.2.2 Parabolic Trough Collector Systems . . . 3
  - 1.2.3 Parabolic Dish Collectors . . . 4
  - 1.2.4 Solar Power Tower Systems . . . 5
- 1.3 Technical Comparison of CSP Technologies . . . 6
  - 1.3.1 Linear-Focusing Technologies . . . 7
  - 1.3.2 Point-Focusing Technologies . . . 7

2 Power Production: Organic Rankine Cycle 9
- 2.1 Rankine Cycle . . . 9
- 2.2 Organic Rankine Cycle . . . 11
- 2.3 Organic Working Fluids . . . 13
  - 2.3.1 Slope of the Saturated Vapour Curve . . . 13
  - 2.3.2 Latent Heat of Vaporization, Density and Specific Heat . . . 14
  - 2.3.3 Viscosity and Conductivity . . . 15
  - 2.3.4 Critical Temperature and Pressure . . . 15
  - 2.3.5 Chemical Stability and Material Compatibility . . . 16
  - 2.3.6 Safety . . . 16
  - 2.3.7 Environmental aspects . . . 16
  - 2.3.8 Availability and cost . . . 17
- 2.4 Working Fluid Selection . . . 18
  - 2.4.1 MDM . . . 19

2.4.2 Toluene . . . 19
2.4.3 D4 . . . 20
2.4.4 Dowtherm-A . . . 21

3 Modeling of ORC System 22
3.1 Solar-Driven ORC Modeling . . . 22
3.2 Component Modeling . . . 24
3.2.1 Turbine . . . 24
3.2.2 Condenser . . . 27
3.2.3 Pump . . . 31
3.2.4 Evaporator . . . 33
3.3 Base ORC Model . . . 39
3.3.1 MDM Base ORC Configuration . . . 39
3.3.2 Toluene Base ORC Configuration . . . 41
3.3.3 D4 Base ORC Configuration . . . 42
3.4 Regenerative ORC Model . . . 43
3.4.1 MDM Regenerative ORC Configuration . . . 44
3.4.2 Toluene Regenerative ORC Configuration . . . 48
3.4.3 D4 Regenerative ORC Configuration . . . 51

4 Solar Field Modeling and ORC Performance 54
4.1 Solar Field Operating Conditions . . . 54
4.2 Solar Field Sizing . . . 57
4.3 Configuration Comparison . . . 59

5 Economic Assessment of the Plant 62
5.1 Cost Estimation Methodology . . . 62
5.1.1 Estimation of BEC . . . 63
5.1.2 Estimation of EPCC . . . 67
5.1.3 Estimation of TPC . . . 67
5.1.4 Estimation of TOC . . . 68
5.1.5 Estimation of TASC . . . 68
5.2 Economic Performance Evaluation . . . 69
5.2.1 Discount Rate Estimation . . . 69
5.2.2 Annual Savings and Incentives . . . 72
5.2.3 Net Present Value Results . . . 75

6 Conclusions 79

Bibliography 81

List of Tables

1.1 Comparison of linear-focusing CSP technologies 7
1.2 Comparison of point-focusing CSP technologies 7

2.1 Safety classification of working fluids 16
2.2 Indicative fluid cost ranges 17
2.3 Selected working fluids 18

3.1 Turbine modeling assumptions 26
3.2 Turbine sensitivity analysis results 27
3.3 Condenser modeling assumptions 31
3.4 Condenser sensitivity analysis results 31
3.5 Pump modeling assumptions 32
3.6 Pump modeling results 33
3.7 Evaporator modeling assumptions 38
3.8 Evaporator sensitivity analysis results 38
3.9 Main results of the MDM regenerative ORC cycle 48
3.10 Main results of the Toluene regenerative ORC cycle 50
3.11 Main results of the D4 regenerative ORC cycle 53

4.1 Seasonal operating hours of the solar-driven ORC system 55
4.2 Seasonal direct normal irradiance values 56
4.3 Daily and seasonal operating time 56
4.4 Annual operating hours and direct normal irradiance 56
4.5 Evaporator thermal load for the analyzed ORC configurations . . . 57
4.6 Useful thermal power provided by a single solar collector 57
4.7 Required number of parabolic dish collectors 58
4.8 Required solar field aperture area 58
4.9 Efficiency comparison between base and regenerative configurations 60

5.1 Contribution of each component to the total equipment cost 67
5.2 Estimated capital costs for both configurations 69
5.3 Annual savings and incentives 75

5.4 Cash-flow analysis for the base case scenario 75
5.5 Cash-flow analysis for the regenerative case scenario 76
5.6 Additional economic indicators for the base case scenario 78

List of Figures

1.1 Main configurations of Concentrated Solar Power plants 2
1.2 Linear Fresnel Reflector system representation 3
1.3 Schematic of Solar Parabolic Trough Collector 4
1.4 Parabolic Dish Solar Concentrator model 5
1.5 Solar Power Tower system 6

2.1 Basic layout of a Rankine cycle power plant 9
2.2 T-s diagram of the ideal Rankine cycle 10
2.3 Basic ORC layout and T-s diagram 12
2.4 Saturated vapor curves for wet, dry and isentropic working fluids . . 14
2.5 T-s diagram of MDM 19
2.6 T-s diagram of Toluene 20
2.7 T-s diagram of D4 21

3.1 Solar parabolic dish prototype installed at the Energy Center 22
3.2 Average seasonal temperature reached at the receiver focus 23
3.3 MDM - Turbine modeling and sensitivity analysis in Aspen Plus . . 25
3.4 Toluene - Turbine modeling and sensitivity analysis in Aspen Plus . 25
3.5 D4 - Turbine modeling and sensitivity analysis in Aspen Plus 26
3.6 MDM - Condenser modeling and sensitivity analysis in Aspen Plus 28
3.7 MDM - Temperature profiles in the condenser 28
3.8 Toluene - Condenser modeling and sensitivity analysis in Aspen Plus 29
3.9 Toluene - Temperature profiles in the condenser 29
3.10 D4 - Condenser modeling and sensitivity analysis in Aspen Plus . . 30
3.11 D4 - Temperature profiles in the condenser 30
3.12 Pump - Aspen Plus scheme 32
3.13 MDM - Evaporator modeling and sensitivity analysis in Aspen Plus 34
3.14 MDM - Temperature profiles in the evaporator 35
3.15 Toluene - Evaporator modeling and sensitivity analysis in Aspen Plus 35
3.16 Toluene - Temperature profiles in the evaporator 36
3.17 D4 - Evaporator modeling and sensitivity analysis in Aspen Plus . . 37

3.18 D4 - Temperature profiles in the evaporator 37
3.19 T-s diagram of the base ORC cycle using MDM 39
3.20 Aspen Plus layout of the MDM-based ORC system 40
3.21 T-s diagram of the base ORC cycle using Toluene 41
3.22 Aspen Plus layout of the Toluene-based ORC system 41
3.23 T-s diagram of the base ORC cycle using D4 42
3.24 Aspen Plus layout of the D4-based ORC system 43
3.25 Regenerative ORC scheme and T-s diagram [10] 43
3.26 Aspen Plus layout of the MDM-based regenerative ORC system . . 44
3.27 MDM - bleeding sensitivity analysis 45
3.28 T-s diagram of the regenerative ORC cycle using MDM 46
3.29 Toluene bleeding sensitivity analysis 48
3.30 Aspen Plus layout of the Toluene-based regenerative ORC system . 49
3.31 T-s diagram of the regenerative ORC cycle using Toluene 50
3.32 D4 bleeding sensitivity analysis 51
3.33 Aspen Plus layout of the D4-based regenerative ORC system 52
3.34 T-s diagram of the regenerative ORC cycle using D4 52

4.1 Seasonal focal temperature profiles with operating threshold 55

5.1 NPV trend for the base case scenario 76
5.2 NPV trend for the regenerative case scenario 77

Acronyms

ORC Organic Rankine Cycle

CSP Concentrated Solar Power

HTF Heat Transfer Fluid

MDM Octamethyltrisiloxane

D4 Octamethylcyclotetrasiloxane

DNI Direct Normal Irradiance

PDC Parabolic Dish Collector

ODP Ozone Depletion Potential

GWP Global Warming Potential

NETL National Energy Technology Laboratory

BEC Bare Erected Cost

EPCC Engineering, Procurement and Construction Cost

TPC Total Plant Cost

TOC Total Overnight Cost

TASC Total As-Spent Cost

NPV Net Present Value

WACC Weighted Average Cost of Capital

Chapter 1

Solar Energy: Concentrated Solar Power Systems

1.1 General overview

In recent years, the global electricity sector has been undergoing a profound transformation. This change is mainly driven by the continuous growth in electricity demand and by the urgent need to reduce emissions associated with power generation. According to the International Energy Agency, global electricity demand is expected to increase by an average of 3.6% per year between 2026 and 2030. This growth is mainly linked to the expansion of industrial activities, the increasing use of electric vehicles, the spread of air conditioning systems and the rapid development of data centres. At the same time, renewable energy sources are expected to become increasingly important in the global power mix. Renewable electricity generation is forecast to grow by approximately 1000 TWh per year up to 2030, showing the central role that clean energy technologies will play in the coming decades. In this context, the development of efficient, flexible and reliable energy systems becomes essential. Such systems must be able to integrate renewable sources effectively, while ensuring a stable and sustainable electricity supply [1].

Long-term projections indicate that, by 2050, renewable sources could provide around 85% of global electricity generation. Within this scenario, wind and photovoltaic technologies are expected to give the largest contribution. Concentrated Solar Power (CSP), on the other hand, could account for about 4% of global electricity production. Although this share is lower than that of other renewable technologies, CSP remains particularly interesting because of its ability to provide dispatchable solar energy, especially when coupled with thermal energy storage systems. According to the roadmap proposed by the International Energy Agency, with adequate policy support and technological development, CSP could supply

up to 11.3% of global electricity demand by 2050. Of this amount, 9.6% would come directly from solar energy, while the remaining 1.7% would be provided by backup systems, such as biomass or fossil fuels. This highlights the potential role of CSP not only as a renewable energy technology but also as a solution capable of improving the flexibility and reliability of future electricity systems [2].

1.2 Classification of CSP systems

Concentrated Solar Power plants can be classified according to the optical configuration used to collect and concentrate solar radiation. In general, CSP systems use reflective surfaces to concentrate Direct Normal Irradiance (DNI) onto a receiver. In the receiver, solar radiation is converted into thermal energy and then transferred to a heat transfer fluid, which can be used to produce electricity or stored for later use. The main commercial CSP technologies are usually divided into four categories: Parabolic Trough Collectors, Linear Fresnel Reflectors, Solar Power Towers and Parabolic Dish systems. Parabolic trough collectors and Linear Fresnel reflectors are classified as linear focusing technologies, since they concentrate solar radiation along a receiver tube. Solar towers and parabolic dishes, instead, are classified as point focusing technologies because they concentrate the incoming radiation onto a single receiver point. This distinction has an important influence on the performance and possible applications of each technology. In particular, the optical configuration affects the concentration ratio, operating temperature, overall efficiency, plant size, and suitability for thermal energy storage. Linear focusing systems are generally more mature and are widely adopted in large-scale CSP plants. Point focusing systems, on the other hand, can reach higher temperatures and higher concentration ratios, making them especially interesting for advanced and high-efficiency power cycles. The following sections describe the main CSP technologies in more detail, focusing on their operating principles, main advantages, and limitations [3].

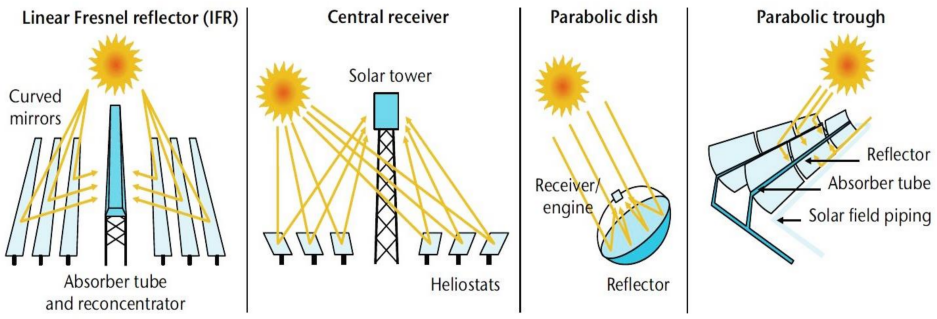


Figure 1.1: Main configurations of Concentrated Solar Power plants [3]

1.2.1 Linear Fresnel Reflector Systems

Linear Fresnel collectors are concentrating solar systems in which direct solar radiation is reflected by a field of flat or slightly curved mirrors towards a fixed receiver positioned above the mirror field. The mirrors are arranged in parallel rows and rotate around their own axis through a solar tracking system. In this way, they follow the apparent movement of the Sun during the day and continuously direct the reflected rays onto the receiver.

Inside the receiver, one or more absorber tubes are crossed by a heat transfer fluid. The concentrated radiation is absorbed by these tubes and converted into thermal energy, increasing the temperature of the fluid flowing inside them. The collected heat can then be used to produce steam for electricity generation, to supply industrial processes, or to be stored in thermal energy storage systems.

One of the main features of Linear Fresnel collectors is that only the mirrors move, while the receiver remains fixed. This makes the system mechanically simpler than other concentrating solar technologies, reducing the number of moving components and making maintenance easier [4].

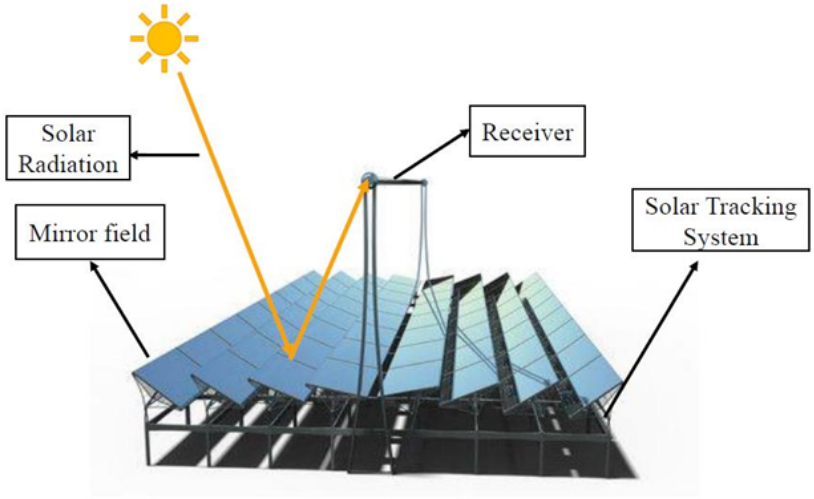


Figure 1.2: Linear Fresnel Reflector system representation [4]

1.2.2 Parabolic Trough Collector Systems

Parabolic Trough Collectors are one of the most established technologies used in Concentrated Solar Power systems. They are made of a parabolic mirror that reflects and concentrates direct solar radiation onto a receiver tube placed along the

focal line of the collector. A heat transfer fluid flows inside this tube and absorbs the thermal energy produced by the concentrated sunlight.

To reduce heat losses, the receiver tube is usually surrounded by a glass envelope, often with an evacuated space between the tube and the glass. The absorber surface is also coated with selective materials, which help increase the absorption of solar radiation and reduce thermal emission. In this way, the collected heat can be transferred more efficiently to the fluid. During operation, the collector follows the apparent movement of the Sun through a tracking system. This allows the reflected rays to remain focused on the receiver tube for most of the day, improving the amount of useful thermal energy collected. The heated fluid can then be used for different applications, such as steam generation, industrial heat supply or electricity production through thermodynamic cycles. For these reasons, Parabolic Trough Collectors represent a mature and reliable solution for medium- and high-temperature solar thermal applications [5].

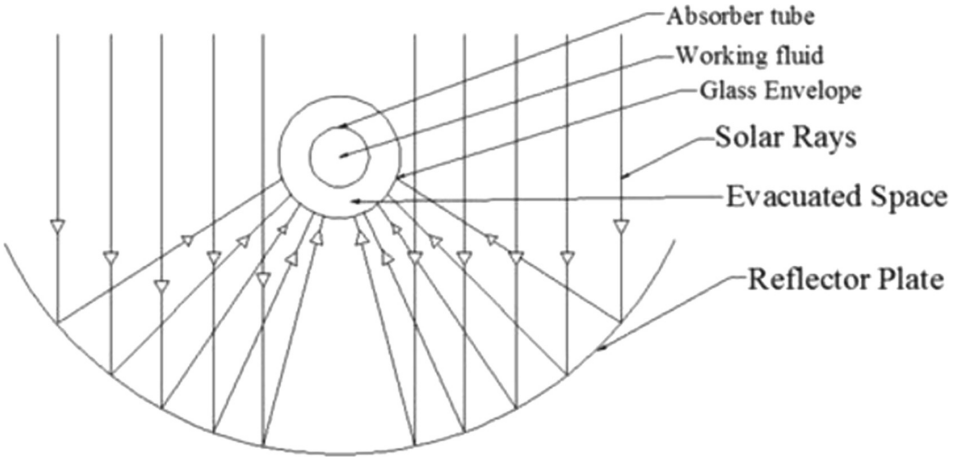


Figure 1.3: Schematic of Solar Parabolic Trough Collector [5]

1.2.3 Parabolic Dish Collectors

Parabolic Dish Collectors (PDCs) are concentrating solar systems that use a parabolic reflective surface to collect direct solar radiation and focus it onto a receiver placed at the focal point. At this point, the concentrated solar energy is absorbed and converted into thermal energy, which can then be transferred to a working fluid and used in different energy conversion systems. Their operation strongly depends on the accurate alignment between the dish, the Sun and the receiver; for this reason, PDCs usually require a two-axis tracking system, which allows the concentrator to follow the apparent motion of the Sun throughout the day and maintain the solar flux on the receiver.

From a performance point of view, PDCs are characterized by high concentration ratios and by the possibility of reaching very high operating temperatures. However, their overall efficiency is closely related to the optical quality of the reflecting surface, the precision of the tracking system, the geometry and position of the receiver, and the reduction of thermal losses due to convection and radiation. A proper receiver design is particularly important, since it affects the distribution of the concentrated solar flux and helps avoid local overheating phenomena that may reduce the reliability and efficiency of the system.

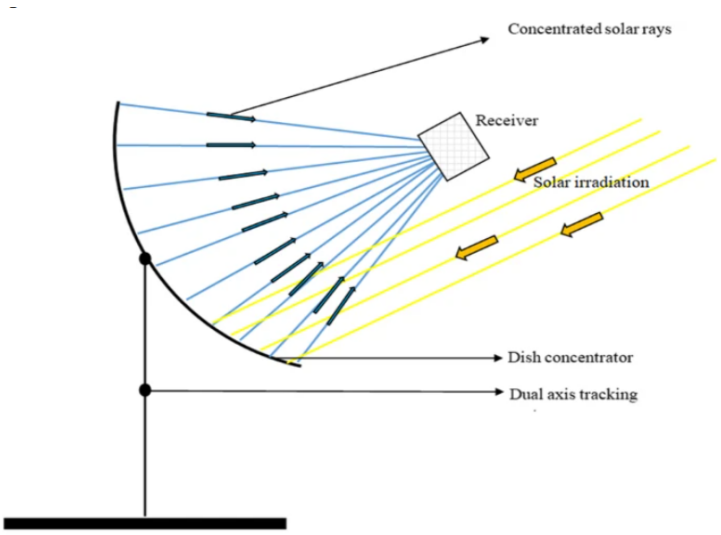


Figure 1.4: Parabolic Dish Solar Concentrator model [6]

Thanks to these characteristics, PDCs are suitable for applications requiring high-temperature thermal energy. They can be coupled with Stirling engines, microturbines and thermodynamic cycles, including the Rankine cycle and the Organic Rankine Cycle (ORC), where the heat supplied by the solar collector is used to produce mechanical work and, subsequently, electricity. In addition, PDCs can also be applied to desalination, hydrogen production and other industrial thermal processes [6].

1.2.4 Solar Power Tower Systems

A solar power tower plant produces electricity by using solar radiation as a heat source. A large field of heliostats, made up of mirrors that follow the Sun during the day, reflects direct solar radiation towards a receiver located at the top of a central tower. In the receiver, the concentrated radiation is absorbed and transferred to a heat transfer fluid, usually molten salts, which can reach high temperatures.

The molten salts are then sent either to a thermal storage tank or directly to the steam generation system. Their use is particularly advantageous because they can both transport and store heat, allowing the plant to produce electricity even when solar radiation is reduced or temporarily unavailable.

When power generation is required, the hot molten salts transfer their heat to water through heat exchangers, producing superheated steam. This steam is then expanded in a turbine connected to an electric generator, as in a conventional Rankine cycle. After expansion, the steam is condensed and pumped back to the steam generation section, completing the cycle.

In this way, a solar power tower plant combines solar concentration, thermal storage and a conventional steam power block, making it possible to convert solar energy into electricity in a more flexible and continuous way [7].

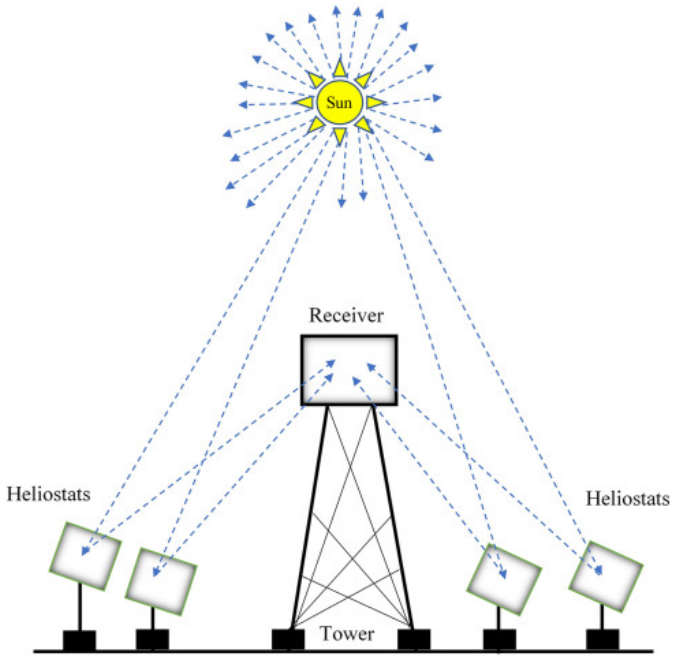


Figure 1.5: Solar Power Tower system [8]

1.3 Technical Comparison of CSP Technologies

To compare the CSP configurations described in the previous sections, the main technologies are divided into linear and point focusing systems. The comparison is based on optical efficiency, operating temperature range and the main design features that determine their suitability for different applications.

The values presented in the following tables represent typical average ranges reported in the literature and should therefore be regarded as indicative rather than as fixed limits. Actual performance may differ depending on the collector design, receiver configuration, tracking accuracy, operating conditions and properties of the heat-transfer fluid.

1.3.1 Linear-Focusing Technologies

Linear-focusing systems concentrate direct solar radiation along a tubular receiver. Parabolic trough collectors and linear Fresnel reflectors are the two main technologies belonging to this category. Their typical optical efficiencies and operating temperature ranges are compared in Table 1.1.

	PTC	**LFR**
Optical efficiency	60-75%	45-60%
HTF operating temperature	350-400 °C	270-500 °C

Table 1.1: Comparison of linear-focusing CSP technologies[4, 5]

Parabolic trough collectors generally achieve higher optical efficiencies because their continuous parabolic surface concentrates the incident radiation more effectively onto the receiver tube.

Linear Fresnel reflectors instead consist of several rows of flat or slightly curved mirrors, resulting in a simpler collector geometry. However, their optical performance is usually lower because of shading, blocking and cosine losses. Despite these limitations, their broad operating temperature range allows their use in several medium and high temperature solar thermal applications.

1.3.2 Point-Focusing Technologies

Point-focusing technologies concentrate direct solar radiation onto a relatively small focal area. This configuration allows higher concentration ratios and, consequently, higher operating temperatures than those generally obtained with linear-focusing systems.

	PDC	**SPT**
Optical efficiency	80-90%	50-75%
HTF operating temperature	250-1000 °C	290-565 °C

Table 1.2: Comparison of point-focusing CSP technologies [6, 7]

Parabolic dish collectors generally achieve the highest optical efficiencies among CSP technologies and can operate over a wide temperature range. These characteristics result from their high concentration ratio and accurate two-axis tracking system. Moreover, their modular configuration makes them particularly suitable for small-scale systems and distributed power-generation applications.

Solar power tower systems are instead mainly intended for large-scale installations, in which a field of independently controlled heliostats directs the incident solar radiation towards a central receiver. Their overall optical performance can be affected by cosine, shading, blocking and atmospheric attenuation losses. Nevertheless, the central-receiver configuration enables high-temperature operation and can be effectively integrated with thermal energy storage.

The comparison therefore does not identify a universally superior technology, since the most appropriate configuration depends on the required temperature level, plant capacity and intended application. For the small-scale solar-driven system investigated in this work, the parabolic dish collector is considered the most suitable solution because of its high optical efficiency, wide operating temperature range and modular configuration.

Chapter 2

Power Production: Organic Rankine Cycle

2.1 Rankine Cycle

The Rankine cycle is one of the most widely used thermodynamic cycles for power generation. Its main purpose is to convert thermal energy into mechanical work and, subsequently, into electrical energy. For this reason, it represents the basic operating principle of many conventional power plants. It is also the reference configuration for ORC systems, where an organic working fluid is used instead of water in order to operate more effectively with low- and medium-temperature heat sources.

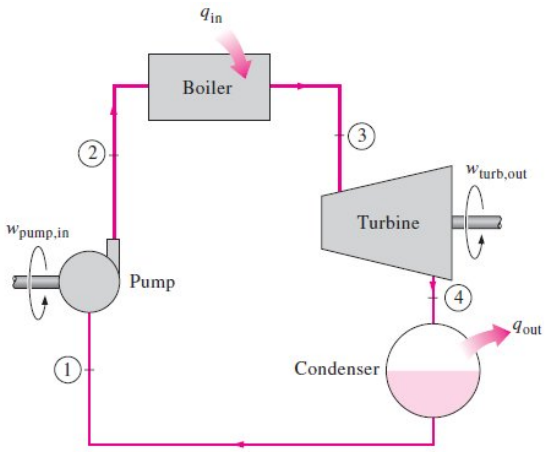


Figure 2.1: Basic layout of a Rankine cycle power plant [9]

Although the layout of the cycle is relatively simple, its importance lies in the possibility of converting heat supplied from an external source into useful power through a closed sequence of thermodynamic processes. The same working fluid circulates continuously within the plant, undergoing changes in pressure, temperature and physical state as it passes through the different components.

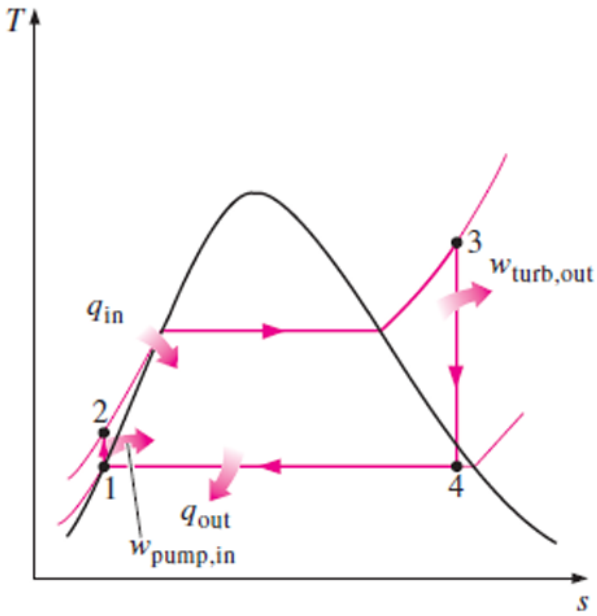


Figure 2.2: T-s diagram of the ideal Rankine cycle [9]

With reference to the temperature–entropy diagram shown in Figure 2.2, the ideal Rankine cycle can be described through the following thermodynamic transformations:

- **1–2: Compression in the pump.** The working fluid enters the pump as a saturated or subcooled liquid and its pressure is increased. Since the fluid is in liquid state, the specific work required by the pump is usually much lower than the work produced by the turbine.
- **2–3: Heat addition in the boiler.** The pressurized liquid receives heat from the external source. During this process, the fluid is first heated up to the saturation condition and then evaporated, becoming high-pressure vapor.
- **3–4: Expansion in the turbine.** The high-pressure vapour expands through the turbine, producing useful mechanical work. During the expansion, both pressure and temperature decrease.

- **4–1: Heat rejection in the condenser.** After leaving the turbine, the working fluid enters the condenser, where heat is rejected to the external environment. The vapor is condensed back into liquid, restoring the initial condition of the cycle.

From a thermodynamic point of view, these four transformations define the main energy exchanges of the Rankine cycle. The T-s diagram is particularly useful because it clearly shows how the working fluid evolves during compression, heating, expansion and condensation. In this way, each point of the cycle can be associated with a specific thermodynamic state and with a specific component of the plant. The overall performance of the cycle mainly depends on the work produced by the turbine, the work required by the pump and the amount of heat supplied in the boiler. In general, the efficiency of a Rankine cycle is strongly influenced by the selected pressure and temperature levels, as well as by the thermodynamic properties of the working fluid. For this reason, the choice of the operating conditions and of the working fluid is especially important in low- and medium-temperature applications, such as solar thermal systems and ORC.

2.2 Organic Rankine Cycle

The growing concern about climate change and the continuous increase in CO_2 emissions related to the intensive use of fossil fuels have made the development of more sustainable energy technologies increasingly urgent. In 2021 alone, according to the International Energy Agency, global energy-related CO_2 emissions reached 36.3 gigatonnes [10].

At the same time, large amounts of industrial waste heat are still released into the environment without being recovered or reused. For example, in the United States, the unrecovered waste heat potential below 150 °C has been estimated at about 75×10^9 kWh/year, mainly originating from furnaces, dryers, heat exchangers and combustion systems [10]. In this context, ORCs represent a promising technology for improving the overall efficiency of energy systems. Unlike conventional Rankine cycles, which generally use water as the working fluid, ORC systems employ organic fluids characterized by a lower boiling point.

This allows them to operate effectively with low- and medium-temperature heat sources, making them particularly suitable for applications where traditional steam cycles would be less efficient or technically less convenient.

The basic layout of an Organic Rankine Cycle is shown in Figure 2.3. The system is based on the same general principle as a conventional Rankine cycle, but the use of an organic working fluid strongly affects the thermodynamic behaviour of the cycle.

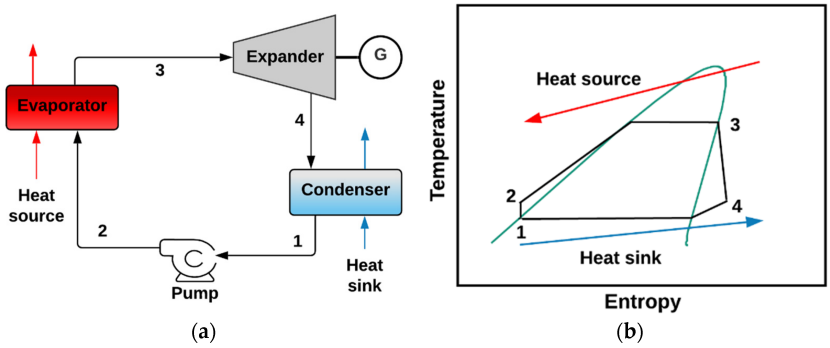


Figure 2.3: Basic ORC layout and T-s diagram [10]

As can be observed from the T-s diagram, the expansion process does not end inside the two-phase region. Instead, the working fluid remains in dry or superheated vapour conditions at the turbine outlet. This behaviour is a typical feature of many ORC systems, especially when dry or isentropic fluids are used. During the expansion, these fluids tend to avoid the wet vapour region, reducing the risk of liquid droplet formation inside the turbine.

This aspect is particularly important because the presence of droplets could damage the turbine blades and reduce the reliability of the expander. Therefore, the figure does not only describe the basic operation of the ORC, but also highlights one of its main advantages: the expansion can be completed under dry or superheated vapour conditions, improving the safety and durability of the system.
The main fields of application of ORC systems include:

- recovery of industrial waste heat from processes such as furnaces, dryers, heat exchangers and combustion systems;
- exploitation of low-enthalpy geothermal resources;
- integration with solar thermal plants;
- recovery of thermal energy from exhaust gases of internal combustion engines and gas turbines.

2.3 Organic Working Fluids

The selection of the working fluid is one of the key aspects in the design of an ORC, since it directly affects both the thermodynamic performance of the system and its compatibility with the available heat source. A first important criterion is the classification of the fluid as wet, dry or isentropic, which depends on the slope of the saturation vapour curve in the T-s diagram. This characteristic is particularly relevant because it influences the need for superheating and the vapour quality at the outlet of the expander. However, the choice of the fluid cannot be based on this aspect alone. Other thermophysical properties, such as specific enthalpy, critical temperature and pressure, latent heat of vaporization and maximum thermal stability temperature, must also be carefully considered. In addition, chemical stability, operational safety, commercial availability and environmental impact play an important role. The latter is generally evaluated through indicators such as the Ozone Depletion Potential (ODP) and the Global Warming Potential (GWP). Finally, the working fluid must be selected according to the temperature level of the heat source, since the performance of each fluid can vary significantly over the operating temperature range [11]. For this reason, fluid selection in ORC systems requires a balanced approach that combines thermodynamic performance, practical operating requirements and environmental constraints.

2.3.1 Slope of the Saturated Vapour Curve

The slope of the saturated vapour curve in the T-s diagram is one of the most important criteria in the selection of organic working fluids for ORC systems. This property strongly affects the behaviour of the fluid during the expansion process and, consequently, determines whether superheating is required before the turbine. According to the shape of the saturation curve, working fluids are generally classified as wet, dry or isentropic fluids:

- **Wet fluids** are characterized by a negative slope of the saturated vapour curve. During the expansion process, these fluids tend to enter the two-phase region, leading to the formation of liquid droplets at the turbine outlet. This condition can cause erosion and mechanical damage to the turbine blades. For this reason, wet fluids usually require a significant degree of superheating, which increases both system costs and thermodynamic irreversibilities.

- **Dry fluids** have a positive slope of the saturated vapour curve. In this case, the fluid leaves the turbine in a superheated vapour state, avoiding the risk of liquid droplet formation and turbine erosion. However, the presence of residual superheat at the turbine outlet may represent an unused amount of

thermal energy. Therefore, dry fluids are often combined with a regenerator in order to recover part of this heat and improve the overall cycle efficiency.

- **Isentropic fluids** present an almost vertical saturated vapour curve in the T-s diagram. They are generally considered a favourable compromise, since the expansion process occurs close to the saturation line without significant liquid formation or excessive superheating at the turbine outlet. As a result, they can reduce the need for additional components and simplify the plant configuration [12].

For these reasons, the slope of the saturated vapor curve is a useful preliminary indicator for evaluating the suitability of a working fluid in an ORC system, especially when considering turbine protection, heat recovery requirements and overall plant complexity.

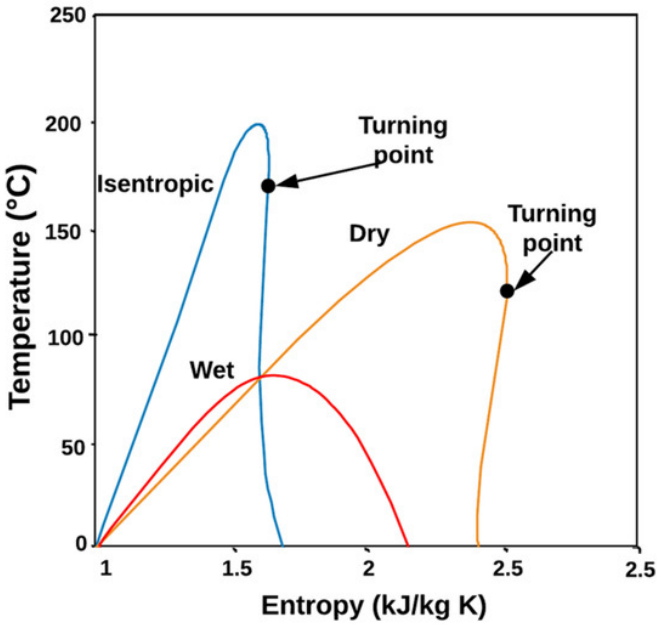


Figure 2.4: Saturated vapor curves for wet (red), dry (orange), and isentropic (blue) working fluids [10]

2.3.2 Latent Heat of Vaporization, Density and Specific Heat

The selection of the working fluid is one of the most important factors affecting the performance of an ORC system, since several thermophysical properties directly influence both the power produced by the turbine and the overall efficiency of the

cycle. In general, fluids with a high latent heat of vaporization are preferred, as they allow a larger pressure difference between evaporation and condensation and, consequently, a greater enthalpy drop during the expansion process.

Fluid density also plays an important role: higher density values make it possible to reduce the mass flow rate required to produce a given power output, with positive effects on the sizing of both the turbine and the pump.

Another relevant property is the specific heat of the liquid phase. A low liquid specific heat reduces the amount of energy required during the preheating process, helping to improve the thermal efficiency of the cycle. Overall, these considerations lead to the preference for fluids characterized by high latent heat, high density and low specific heat, as they help maximize the useful work output while reducing energy losses within the system [13].

2.3.3 Viscosity and Conductivity

In addition to the main thermodynamic properties, the viscosity and thermal conductivity of the working fluid are also important aspects to consider. Low viscosity, both in the liquid and vapor phases, is generally desirable because it helps reduce friction losses in pipes and heat exchangers, improving the hydraulic efficiency of the cycle. At the same time, high thermal conductivity promotes better heat transfer between the fluid and the heat exchanger surfaces. This leads to higher heat transfer coefficients, smaller required exchange areas and, overall, improved plant performance [12].

2.3.4 Critical Temperature and Pressure

The selection of the working fluid requires particular attention to its critical properties, since these parameters define the useful operating range of the cycle and affect the feasibility of both evaporation and condensation processes. A sufficiently high critical temperature is important to allow condensation at practical temperatures and pressures, which is necessary for effective heat rejection to the environment. Fluids with a critical temperature that is too low may operate too close to the critical region or lead to inefficient and impractical condensation conditions, making them less suitable for conventional ORC systems. At the same time, the critical pressure should remain within moderate values: excessively high operating pressures increase plant complexity, costs and safety requirements, making the use of the fluid less attractive. In general, fluids with a high critical temperature and a reasonably low critical pressure provide a favorable compromise between thermodynamic efficiency, simple design and reliable operation [13].

2.3.5 Chemical Stability and Material Compatibility

In the selection of working fluids for ORC and supercritical cycles, chemical stability at operating temperatures is a key aspect to consider. Many organic fluids tend to undergo degradation or chemical decomposition when exposed to high temperatures, which directly limits the maximum temperature that the cycle can safely reach and, consequently, its overall efficiency.

At the same time, the fluid must be compatible with the materials used in the plant and with lubricating oils, in order to avoid corrosion, deposit formation or unwanted chemical reactions. For this reason, the combined evaluation of chemical stability and material compatibility is essential to ensure reliable, safe and long-term operation of the system [13].

2.3.6 Safety

The safety of the working fluid is an important criterion in ORC systems, especially when organic fluids operate at high temperature and pressure. The main risks are related to flammability, toxicity and possible leakage during operation or maintenance. A common reference for classifying fluids is the ASHRAE/ISO safety classification, where the letter indicates the toxicity level and the number indicates the flammability level. Class A refers to lower toxicity fluids, while class B refers to higher toxicity fluids. Flammability is classified from 1 to 3, where 1 indicates no flame propagation and 3 indicates higher flammability [14].

Class	Toxicity level	Flammability level
A1 / B1	Lower / Higher	No flame propagation
A2L / B2L	Lower / Higher	Lower flammability, low burning velocity
A2 / B2	Lower / Higher	Lower flammability
A3 / B3	Lower / Higher	Higher flammability

Table 2.1: Safety classification of working fluids [14]

In addition to this classification, safety can be evaluated through numerical parameters such as flash point, autoignition temperature, lower and upper explosive limits, and occupational exposure limits [13].

2.3.7 Environmental aspects

Environmental aspects are a central criterion in the selection of working fluids for thermodynamic cycles. The main indicators usually considered are the ozone depletion potential (ODP), the global warming potential (GWP) and the atmospheric lifetime, which respectively describe the impact on the ozone layer, the

contribution to climate change and the persistence of the fluid in the atmosphere. International regulations have progressively restricted or phased out many chlorinated and fluorinated refrigerants with high ODP and GWP values, making it necessary to identify alternatives with a lower environmental impact. Among the most promising solutions are fluids containing hydrogen atoms, since they tend to degrade more easily in the lower atmosphere, reducing their lifetime and limiting the probability of reaching the stratosphere. Therefore, environmental assessment cannot be considered a secondary aspect, but rather a design constraint that guides the selection of working fluids towards more sustainable options that comply with current regulations [13].

2.3.8 Availability and cost

A more practical aspect in the choice of a working fluid is its cost and commercial availability. Some refrigerants commonly used in ORC systems can be quite expensive, mainly because their production is complex and their market is still relatively limited. If these fluids were used on a larger scale, their price could decrease over time. However, low-cost hydrocarbons may also be a suitable alternative, since they are generally cheaper and easier to find.

The economic evaluation should not only consider the initial cost of the fluid, but also its availability in the long term. This is important for maintenance, refilling operations and for ensuring the continuous operation of the plant. For this reason, cost and availability represent practical constraints that must be considered together with thermodynamic, safety and environmental aspects when selecting the working fluid [13].

Fluid family	Indicative cost range
Common hydrocarbons and aromatic solvents	1-3 €/kg
Refrigerants	5-30 €/kg
Siloxanes and silicone-based fluids	10-50 €/kg
Commercial heat-transfer fluids	5-20 €/kg

Table 2.2: Indicative fluid cost ranges

The values reported in Table 2.2 are indicative order-of-magnitude estimates and should not be interpreted as fixed market prices. The actual cost of each fluid can vary significantly depending on supplier, purity grade, packaging, purchased quantity and market conditions. Moreover, laboratory-grade prices are usually much higher than bulk industrial prices.

2.4 Working Fluid Selection

Choosing the working fluid is a key step in the development of an ORC, since it directly affects both the performance of the system and the operating conditions of the main components. The thermodynamic properties of the fluid influence the evaporation and condensation processes, the pressure levels of the cycle and the expansion inside the turbine.

For this reason, the selection was carried out by considering the temperature range of the heat source, the critical properties of the fluids, their thermal stability and their environmental impact.
In this work, three organic fluids were selected for the analysis: MDM, Toluene and D4. The choice was made in order to compare fluids with relatively similar critical temperatures, so that their behavior could be evaluated under comparable operating conditions. This makes it possible to understand how each fluid responds within the same ORC layout and which one is more suitable for the system considered.

The main critical properties of the selected working fluids are reported in Table 2.3. As can be observed, the three fluids have close critical temperatures, while their critical pressures differ more significantly. This difference is particularly evident for toluene, which has a higher critical pressure than the two siloxanes. This comparison is useful because the critical properties influence the choice of the evaporation temperature and, consequently, the pressure levels reached in the cycle.

Fluid name	**Fluid type**	T_{crit} [**°C**]	P_{crit} [**bar**]
MDM	Dry	292.21	14.37
Toluene	Isentropic/Dry	318.60	41.26
D4	Dry	313.35	13.47

Table 2.3: Critical temperature and pressure of the selected working fluids

After this preliminary comparison, each fluid was analysed in more detail using Aspen Plus. The evaluation was mainly based on the corresponding T-s diagrams and on the most relevant thermodynamic properties for the cycle.

2.4.1 MDM

The first working fluid analyzed is octamethyltrisiloxane, commonly referred to as MDM, with molecular formula C8H24O2Si3.

It belongs to the family of siloxanes and has a critical temperature of 292.21 °C, and a critical pressure of 14.37 bar [14] [15].

These values are very close to those obtained from Aspen Plus, where the critical temperature is about 290 °C and the critical pressure is 14.34 bar. From the T-s diagram, MDM shows a positive slope of the saturated vapor curve, which classifies it as a dry fluid. This behavior is particularly suitable for ORC applications, since it reduces the risk of liquid formation during the expansion process in the turbine. For this reason, MDM can be considered an appropriate working fluid for the small-scale ORC system analyzed in this study. During the sensitivity analysis, the saturation pressure corresponding to each temperature value was also calculated. The resulting T-s diagram is shown in Figure 2.5.

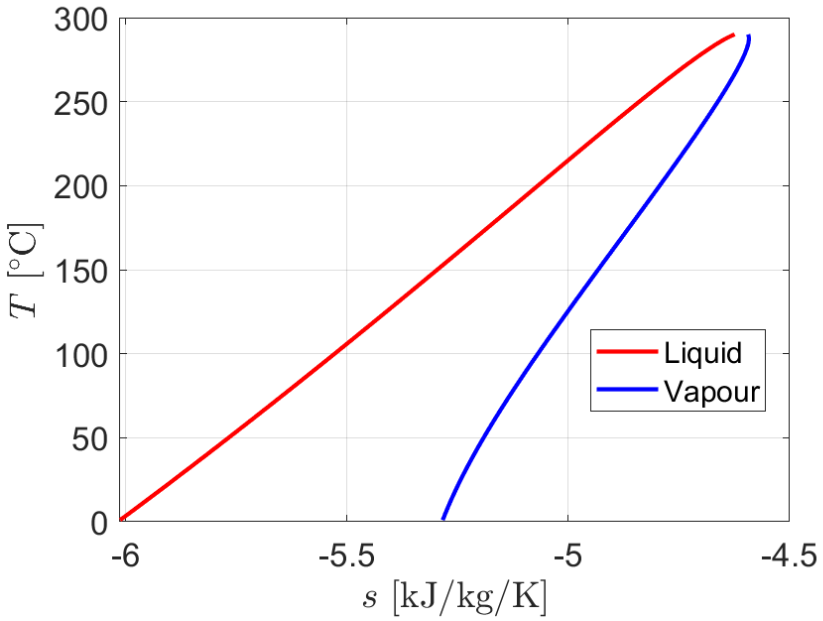


Figure 2.5: T-s diagram of MDM obtained using Aspen Plus

2.4.2 Toluene

Toluene is an organic compound belonging to the family of aromatic hydrocarbons, with the chemical formula C7H8. Its critical temperature is 318.60 °C, while its critical pressure is approximately 41.26 bar [16].

These values are consistent with the thermodynamic properties obtained from Aspen Plus and confirm that toluene can operate in a medium-to-high temperature range. This aspect is particularly relevant for ORC applications, since it allows the fluid to be coupled with heat sources at relatively high temperatures. In addition, toluene is known for its good thermal stability, which makes it suitable for high-temperature ORC systems. From an environmental point of view, it has zero ozone depletion potential and a very low or negligible global warming potential, making it an interesting option among organic working fluids [14]. The T-s diagram obtained for toluene is reported in Figure 2.6.

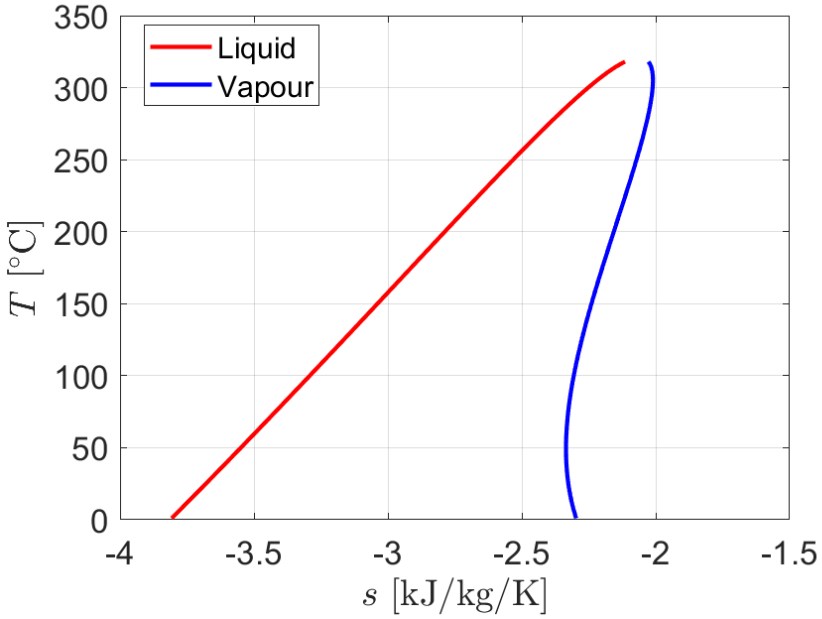


Figure 2.6: T-s diagram of Toluene obtained using Aspen Plus

2.4.3 D4

The third working fluid analyzed is octamethylcyclotetrasiloxane, commonly referred to as D4, with molecular formula C8H24O4Si4. D4 belongs to the family of siloxanes, which are often considered suitable fluids for ORC applications because of their relatively high molecular weight and favorable thermodynamic behavior.

D4 has a critical temperature of 313.35 °C and a critical pressure equal to about 13.47 bar [17]. From the T-s diagram, D4 shows the typical behavior of a dry fluid, with a positive slope of the saturated vapor curve.

For this reason, D4 can be considered an appropriate working fluid for the ORC system analysed in this study. From an environmental point of view, D4 has no

significant ODP effect, while its GWP is very low [14]. The resulting T-s diagram is shown in Figure 2.7.

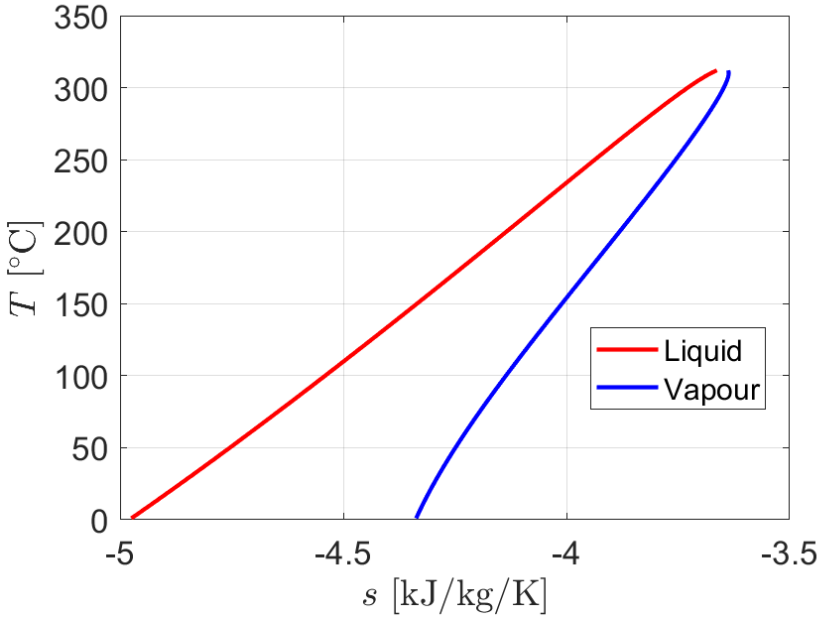


Figure 2.7: T-s diagram of D4 obtained using Aspen Plus

2.4.4 Dowtherm-A

Dowtherm-A was selected as the heat transfer fluid because it is specifically designed for indirect heat transfer applications and can operate over a wide temperature range. It can be used in the liquid phase from 15 °C up to 400 °C, which makes it suitable for the thermal levels considered in the ORC system [18]. Its relatively high boiling point and good thermal stability make it appropriate for transferring heat from the solar concentrator to the ORC evaporator under medium-to-high temperature conditions.

Chapter 3

Modeling of ORC System

3.1 Solar-Driven ORC Modeling

This chapter presents the modeling and simulation of an Organic Rankine Cycle coupled with a solar concentrating system. The study focuses on a 10 kW ORC model, devel oped in Aspen Plus, in order to compare three selected working fluids and identify the one that makes the most effective use of the available solar energy. The solar input is provided by a parabolic dish concentrator installed on the roof of the Energy Center in Turin. The system was designed and manufactured by El.Ma. S.r.l. Electronic Machining for Politecnico di Torino for laboratory testing and research activities.



Figure 3.1: Solar parabolic dish prototype installed at the Energy Center [19]

As shown in Figure 3.1, the concentrator consists of an aluminium paraboloid whose internal surface is covered with a reflective polymeric film, selected to ensure a high optical efficiency. The dish is also equipped with an automatic two-axis tracking system, which controls both azimuth and elevation. In this way, the concentrator can follow the Sun during the day and keep the reflected radiation focused as effectively as possible. The tracking system works by calculating the solar coordinates in real time and continuously adjusting the orientation of the dish.

The paraboloid has a collecting surface of 4.5 m^2 and an optical efficiency of about 80%. Under favourable conditions, the temperature at the focal point can reach very high values, up to approximately 1800 °C. Considering an average direct solar irradiance of about 800 W/m^2, the concentrated power under optimal conditions is around 2.8 kW.

The temperatures reached at the focal point are reported in Figure 3.2. They were obtained starting from the seasonal average irradiance values, which were then used as input data in a two-dimensional COMSOL model. This made it possible to estimate the daily temperature profiles for the different seasons, which are later used as thermal input for the ORC model.

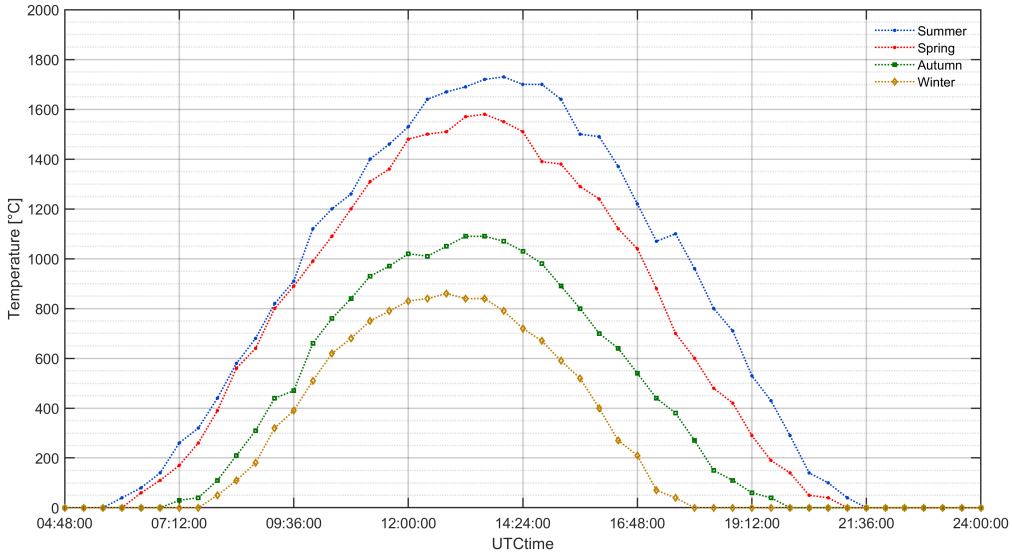


Figure 3.2: Average seasonal temperature reached at the receiver focus

3.2 Component Modeling

In this section, the main components of the ORC system are analyzed separately. For each component, a sensitivity analysis is carried out in order to identify the most suitable design point. In this analysis, one selected parameter is varied within a defined range, while the effect on another relevant parameter is observed. Each simulated process is described through an equivalent mathematical model, made up of linearly independent algebraic and/or differential equations. These equations are formulated so that the number of equations matches the number of unknown variables, allowing the system to be properly solved. The model is based on thermodynamic property balances, phase and chemical equilibrium relationships, transport laws, stoichiometry, kinetic data, and the physical constraints that characterize the process. In this work, the Peng-Robinson equation of state was selected to describe the thermodynamic transformations of the working fluids.

3.2.1 Turbine

The expander is the key component responsible for power production in the system, and for this reason the analysis and modeling were started from this unit. In Aspen Plus, the *Turbine* block from the *Pressure Changers* library was used, defining the inlet conditions according to the thermodynamic properties and operating limits of each working fluid.

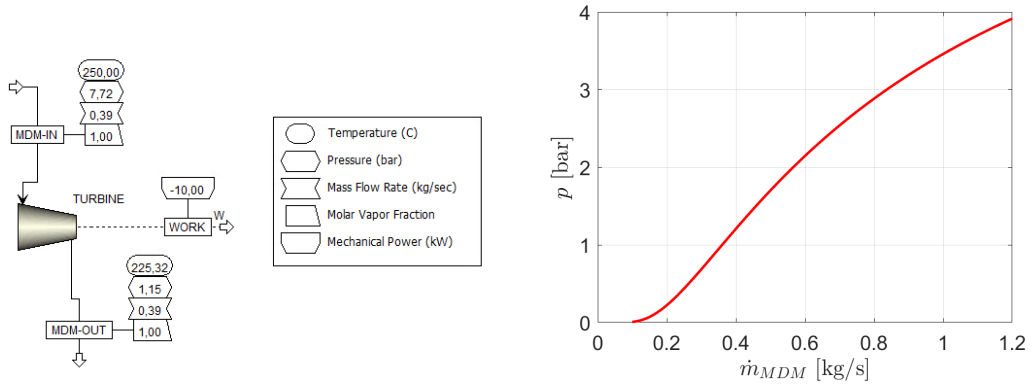
The power output of the expander was set to 10 kW, while the isentropic and mechanical efficiencies were assumed to be 0.90 and 0.98. For each working fluid, a sensitivity analysis was then carried out using the Aspen sensitivity tool. This made it possible to evaluate how the turbine outlet pressure changes with the working fluid mass flow rate and to identify a suitable operating point.

The main objective of this analysis was to make the best possible use of the available enthalpy drop, while keeping the turbine exhaust pressure slightly above atmospheric pressure in order to avoid possible air infiltration into the circuit.

In this work, the turbine inlet temperature was first defined by considering MDM, since this fluid has the lowest critical temperature among the three selected working fluids. The idea was to use the same inlet temperature for all fluids, in order to make the comparison more consistent. For this reason, the temperature at the turbine inlet, corresponding to the outlet of the vapor generator, was set to 250 °C.

This value was chosen because it remains sufficiently below the critical temperature of MDM, which is about 291 °C. In this way, the fluid operates far from critical conditions, avoiding possible instability issues and keeping a reasonable safety margin. At 250 °C, MDM reaches a pressure of about 7.72 bar. A further increase in temperature would also increase the operating pressure, leading to

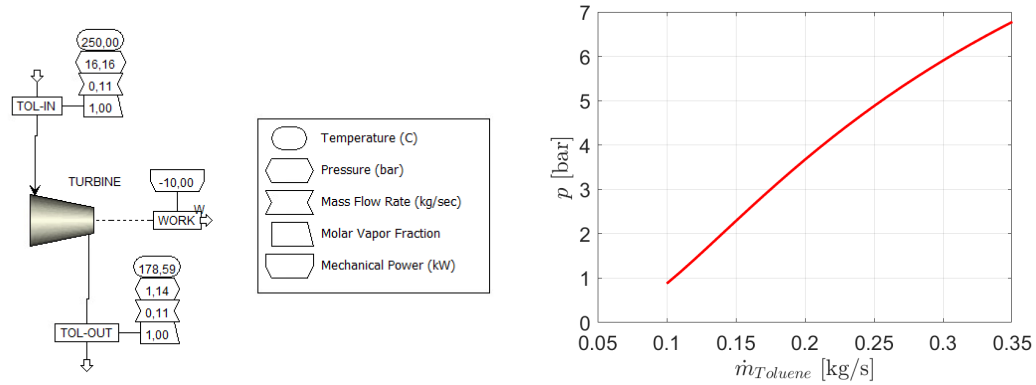
higher pump work and requiring more resistant, and therefore thicker, pipes and components.



(a) Aspen Plus scheme **(b)** Sensitivity analysis

Figure 3.3: MDM - Turbine modeling and sensitivity analysis in Aspen Plus

For toluene, the turbine inlet temperature of 250 °C corresponds to an inlet pressure of about 16.16 bar. The sensitivity analysis was used to identify the most suitable design point for the turbine under the imposed power output of 10 kW. From this analysis, a mass flow rate of about 0.11 kg/s was selected. At this operating point, the outlet conditions are approximately 178.6 °C and 1.14 bar.

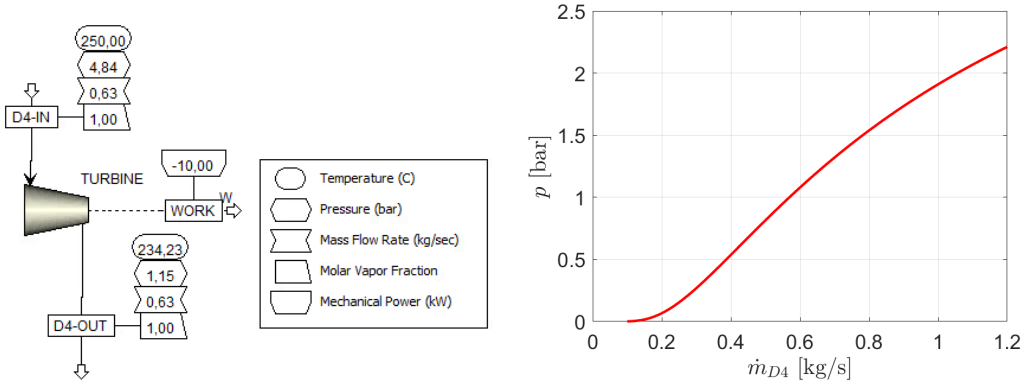


(a) Aspen Plus scheme **(b)** Sensitivity analysis

Figure 3.4: Toluene - Turbine modeling and sensitivity analysis in Aspen Plus

For D4, a turbine inlet temperature of 250 °C corresponds to an inlet pressure of about 4.84 bar, significantly lower than the values obtained for the other two

fluids. The selected operating point requires a mass flow rate of about 0.63 kg/s to produce 10 kW. At the turbine outlet, the temperature is approximately 234.2 °C, while the pressure decreases to about 1.15 bar.



(a) Aspen Plus scheme **(b)** Sensitivity analysis

Figure 3.5: D4 - Turbine modeling and sensitivity analysis in Aspen Plus

The main assumptions adopted for the expander modelling are summarized in Table 3.1. For all the working fluids, the turbine inlet temperature was fixed at 250 °C, while the corresponding inlet pressure was obtained from the thermodynamic properties of each fluid. The mechanical power output was imposed equal to 10 kW, and the same values of isentropic, mechanical and alternator efficiencies were used in order to compare the three cases under consistent modeling conditions.

	MDM	**Toluene**	**D4**
Turbine inlet temperature $T_{\text{turb,in}}$	250 °C	250 °C	250 °C
Turbine inlet pressure $P_{\text{turb,in}}$	7.72 bar	16.16 bar	4.84 bar
Isentropic efficiency $\eta_{\text{is,turb}}$	0.90	0.90	0.90
Mechanical efficiency η_{mec}	0.98	0.98	0.98
Mechanical power output W_{out}	10 kW	10 kW	10 kW
Alternator efficiency η_{al}	0.98	0.98	0.98
Electric power output W_{el}	9.8 kWe	9.8 kWe	9.8 kWe

Table 3.1: Turbine modeling assumptions

The selection of the working fluid mass flow rate was based on the results of the turbine sensitivity analysis, in which the turbine outlet pressure was evaluated as a function of the mass flow rate. The corresponding curves show that, for the three fluids, an increase in mass flow rate leads to an increase in the outlet pressure.

From a practical point of view, working with a lower mass flow rate would be advantageous, since it would reduce the amount of fluid circulating in the system and would also limit the power required by the pump. However, this choice cannot be made only by minimizing the flow rate. If the mass flow rate becomes too low, the turbine outlet pressure may fall below atmospheric pressure, which is not suitable for the operation of the cycle.

For this reason, the final mass flow rate was selected by imposing the same turbine outlet pressure for all the working fluids, equal to about 1.15 bar. This value represents a compromise between keeping the system slightly pressurized and avoiding unnecessarily high mass flow rates. Once this pressure level was fixed, the sensitivity analysis provided the corresponding mass flow rate for each fluid, as reported in Table 3.2. The different values obtained are a direct consequence of the different thermodynamic behavior of the fluids: under the same power output requirement, each fluid needs a different circulating flow rate to provide the required expansion work.

	MDM	**Toluene**	**D4**
Mass flow rate $\dot{m}_{\mathrm{wf}}$	0.39 kg/s	0.11 kg/s	0.63 kg/s
Turbine outlet pressure $P_{\mathrm{turb,out}}$	1.15 bar	1.14 bar	1.15 bar

Table 3.2: Turbine sensitivity analysis results

3.2.2 Condenser

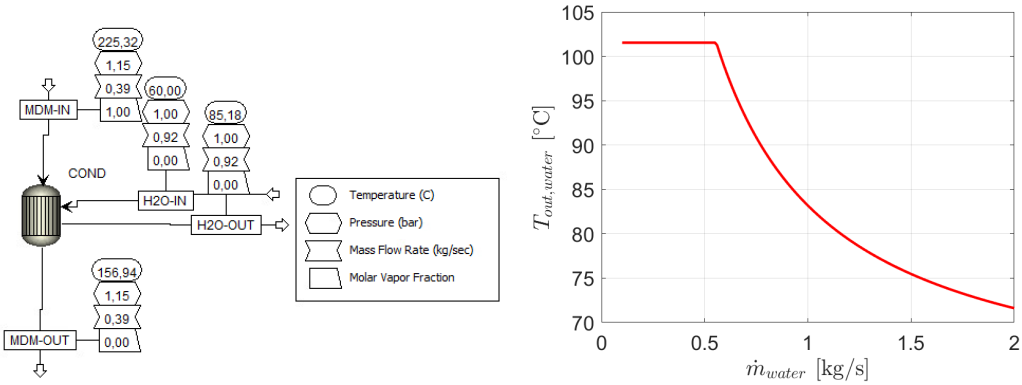
The condenser is the component of the cycle responsible for bringing the hot fluid, namely the working fluid, back to the liquid phase while extracting thermal power from it. It was modeled as a counter-current heat exchanger, where the cold stream is water, which could potentially be used to satisfy an external thermal demand.

In Aspen Plus, the component was simulated using a *HeatX* block from the *Exchangers* library. The inlet conditions of the hot stream correspond to the outlet conditions of the expander discussed in the previous section, while the cooling process was assumed to take place at constant pressure.

For the cold side, water was considered at atmospheric pressure. Its inlet and outlet temperatures were set to 60°C and 85°C, respectively, in order to represent a possible heating application. A sensitivity analysis was then carried out by varying the water mass flow rate and observing its effect on the outlet temperature. This made it possible to identify the flow rate required to achieve the imposed temperature rise across the condenser.

For MDM, the condenser allows the organic fluid to leave the heat exchanger in liquid phase, while the water stream is heated from 60 °C to about 85 °C. The

sensitivity curve in Figure 3.6b shows that the outlet water temperature decreases as the water mass flow rate increases, since the same heat load is transferred to a larger amount of water.



(a) Aspen Plus scheme **(b)** Sensitivity analysis

Figure 3.6: MDM - Condenser modeling and sensitivity analysis in Aspen Plus

Figure 3.7 below shows the temperature profiles of the organic fluid and the water flow inside the condenser. The MDM first cools down from the turbine outlet temperature and then undergoes condensation at constant temperature. At the same time, the water stream absorbs the heat released and is heated from about 60 °C to 85 °C.

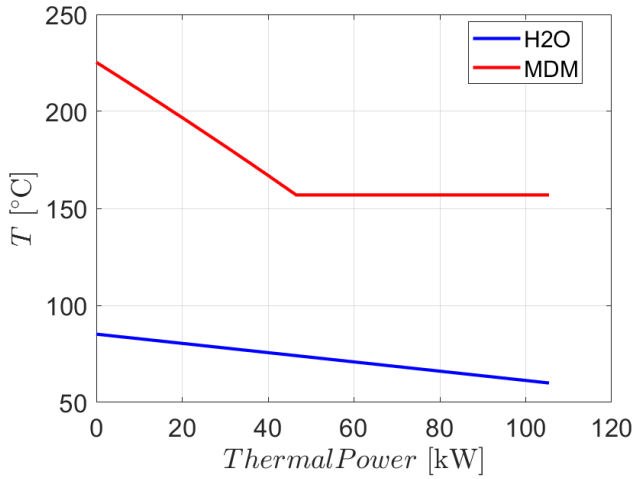
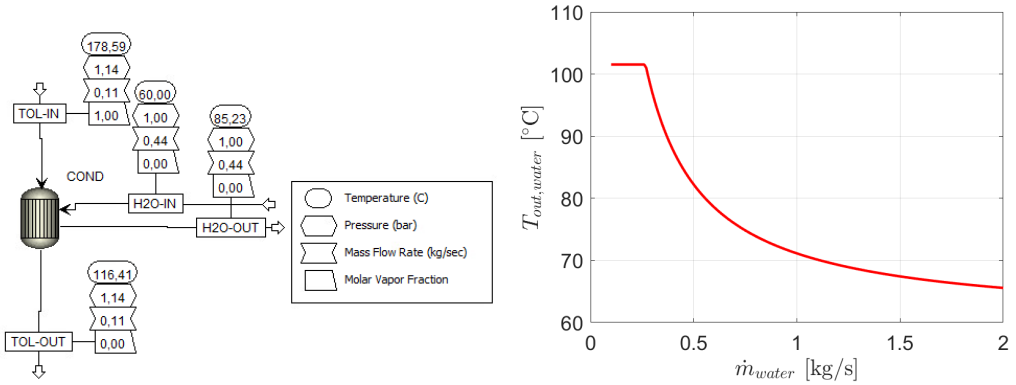


Figure 3.7: MDM - Temperature profiles in the condenser

For Toluene, the condenser operates in the same water temperature range considered

for MDM. However, the required outlet temperature is achieved with a lower water mass flow rate, indicating that less cooling water is needed in this case.



(a) Aspen Plus scheme **(b)** Sensitivity analysis

Figure 3.8: Toluene - Condenser modeling and sensitivity analysis in Aspen Plus

The T–Q diagram for Toluene in Figure 3.9 presents a shorter heat-transfer range than the one obtained for MDM. The organic fluid reaches the condensation region after a limited cooling stage, while the water temperature increases regularly across the condenser. This confirms that the imposed water temperature rise can be achieved with a lower exchanged heat duty.

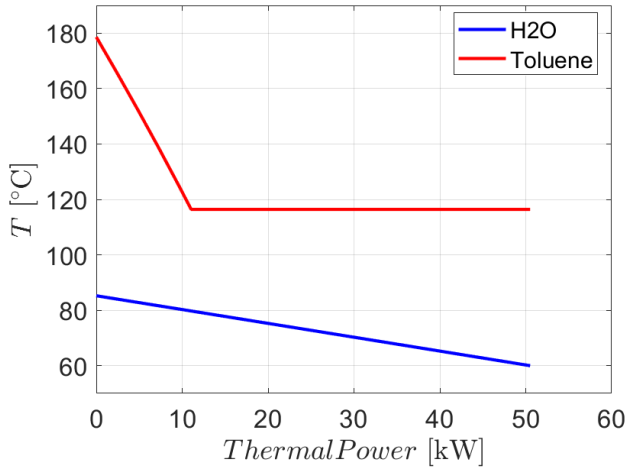
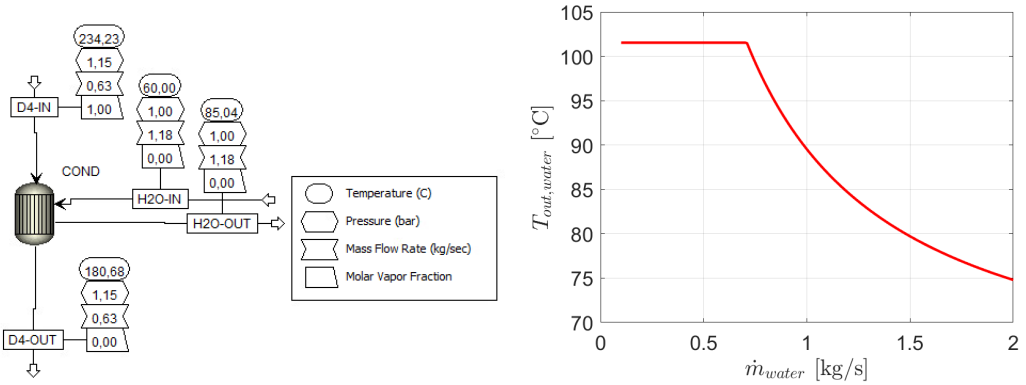


Figure 3.9: Toluene - Temperature profiles in the condenser

For D4, the selected operating point corresponds to a water mass flow rate of about 1.18 kg/s, which allows the outlet water temperature to remain close to the target

value of 85 °C. This value is higher than that obtained for Toluene, showing that the condenser requires a larger water flow in this case.



(a) Aspen Plus scheme **(b)** Sensitivity analysis

Figure 3.10: D4 - Condenser modeling and sensitivity analysis in Aspen Plus

The T–Q diagram for D4 shows the same condensation pattern observed for the other fluids, but over a wider thermal power range. This indicates that a larger amount of heat is transferred to the water stream, which is gradually heated up to the required outlet temperature.

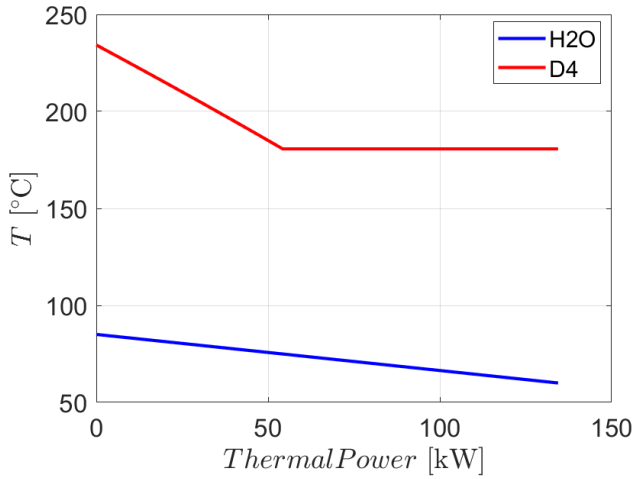


Figure 3.11: D4 - Temperature profiles in the condenser

The main assumptions used for the condenser modeling are summarized in Table 3.3, while the corresponding simulation results are reported in Table 3.4. Once the operating conditions of the hot and cold streams were defined, the simulations

made it possible to evaluate the thermal power rejected by each working fluid and the water mass flow rate required to achieve the imposed temperature increase. The comparison highlights the different condenser behavior associated with MDM, Toluene and D4. In particular, the condenser does not only ensure the complete liquefaction of the organic fluid before the pump inlet, but also allows part of the rejected heat to be recovered as useful thermal energy for possible cogenerative applications.

	MDM	**Toluene**	**D4**
Working fluid mass flow rate $\dot{m}_{wf}$	0.39 kg/s	0.11 kg/s	0.63 kg/s
Condenser inlet temperature $T\text{cond, in}$	225.32 °C	178.59 °C	234.23 °C
Condenser inlet pressure $P_{\text{cond,in}}$	1.15 bar	1.14 bar	1.15 bar
Condenser outlet pressure $P_{\text{cond,out}}$	1.15 bar	1.14 bar	1.15 bar

Table 3.3: Condenser modeling assumptions

The condenser results reported in Table 3.4 highlight clear differences among the three working fluids. D4 provides the highest heat recovery, followed by MDM, while Toluene shows the lowest condenser heat duty and requires the smallest water flow rate. This comparison is particularly relevant because the hot water produced in the condenser may be used for domestic or heating purposes.

	MDM	**Toluene**	**D4**
Mass flow rate $\dot{m}_{water}$	0.92 kg/s	0.44 kg/s	1.18 kg/s
Heat duty $Q\text{cond}$	105.42 kWth	50.51 kWth	134.42 kWth
Outlet temperature $T\text{wf, out}$	156.94 °C	116.41 °C	180.68 °C

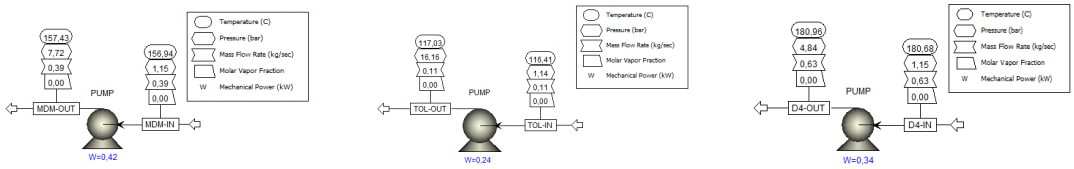
Table 3.4: Condenser sensitivity analysis results

3.2.3 Pump

The pump is used to increase the pressure of the working fluid leaving the condenser, bringing it back to the pressure level required at the turbine inlet. In Aspen Plus, this component was modeled using the *Pump* block available in the Pressure Changers library.

For each working fluid, the inlet conditions of the pump correspond to the outlet conditions obtained from the condenser simulation.

Since the fluid leaves the condenser in liquid phase, the pumping process can be carried out with a relatively low power consumption compared to the turbine output.



(a) MDM **(b)** Toluene **(c)** D4

Figure 3.12: Pump - Aspen Plus scheme

The main assumptions adopted for the pump modeling are reported in Table 3.5. For each working fluid, the inlet pressure of the pump corresponds to the pressure at the condenser outlet, since the pump is placed immediately after the condenser. The outlet pressure was instead set equal to the turbine inlet pressure previously selected for each fluid, in order to bring the working fluid back to the high-pressure side of the cycle. The same isentropic efficiency, equal to 0.90, was assumed for all the cases, so that the comparison between the three fluids could be carried out under consistent modeling conditions.

	MDM	**Toluene**	**D4**
Pump inlet pressure $P_{\text{pump,in}}$	1.15 bar	1.14 bar	1.15 bar
Pump outlet pressure $P_{\text{pump,out}}$	7.72 bar	16.16 bar	4.84 bar
Isentropic efficiency $\eta_{\text{is,pump}}$	0.90	0.90	0.90

Table 3.5: Pump modeling assumptions

Due to the irreversibilities of the pumping process, the working fluid leaves the pump at a slightly higher temperature than at the inlet. However, this temperature variation remains very small for all the analyzed fluids, as can also be observed from the Aspen Plus results.

The pump mainly performs the pressure increase required to bring the fluid back to the turbine inlet conditions, while the thermal state of the fluid changes only slightly.

The main results obtained from the pump simulation are reported in Table 3.6, together with the mechanical power absorbed by the component.

	MDM	**Toluene**	**D4**
Pump outlet temperature $T_{\text{pump,out}}$	157.43 °C	117.03 °C	180.96 °C
Pump mechanical power W_{pump}	0.42 kW	0.24 kW	0.34 kW

Table 3.6: Pump modeling results

3.2.4 Evaporator

The evaporator is the component that allows the ORC to receive thermal energy from the solar section of the plant. In this heat exchanger, the hot stream coming from the solar field transfers heat to the organic working fluid, which is heated and then evaporated before entering the turbine. Therefore, the evaporator represents the connection between the solar field and the power cycle, since the energy collected by the concentrators is supplied to the working fluid through this component.

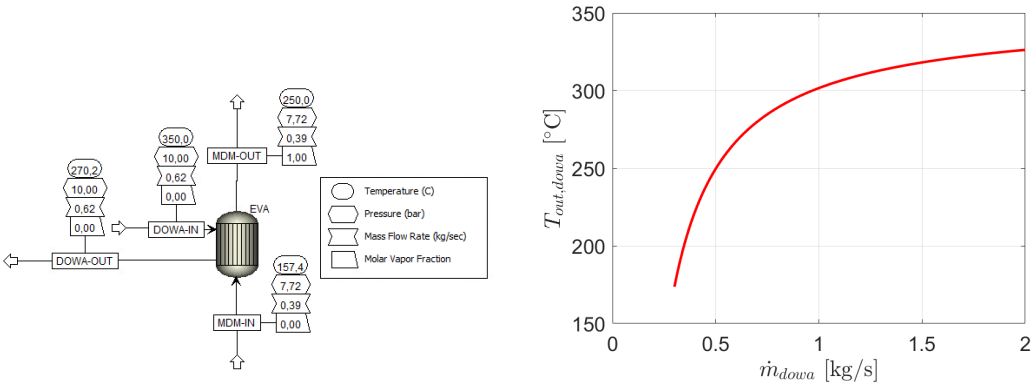
In this study, the evaporator is modeled as a counter-current heat exchanger. The hot side is represented by Dowtherm-A, selected as heat transfer fluid (HTF) for the solar field, while the cold side is the ORC working fluid leaving the pump. This configuration allows the organic fluid to reach the thermodynamic state required at the turbine inlet, while the HTF is cooled as it releases thermal energy.

In Aspen Plus, the evaporator was modeled using the *HeatX* block from the *Exchangers* library. The inlet conditions of the ORC working fluid correspond to the outlet conditions obtained from the pump model, while the outlet conditions were defined according to the turbine inlet state selected in the expander section. During the evaporation process, the pressure of the working fluid was assumed to remain constant, neglecting pressure losses inside the heat exchanger.

Although Dowtherm-A can be used in both liquid-phase and vapor-phase systems, liquid-phase operation was selected in this work. Since the HTF operates in a temperature range higher than its atmospheric boiling point, the solar loop was pressurized to 10 bar in order to keep Dowtherm-A in liquid phase during the heat exchange process. This choice avoids phase change of the HTF inside the evaporator and allows the hot stream to be modeled as a single-phase liquid in Aspen Plus.

The first evaporator model was developed for MDM. The inlet temperature of Dowtherm-A was fixed at 350 °C, according to the operating temperature range considered for the solar field. A sensitivity analysis was then carried out by varying the mass flow rate of the HTF, in order to identify the value required to obtain a temperature decrease of about 80 °C across the evaporator.
The sensitivity curve shows that the outlet temperature of Dowtherm-A increases as the HTF mass flow rate increases. This behavior is expected, since a higher mass flow rate means that the same amount of heat is distributed over a larger quantity of fluid, leading to a smaller temperature drop. On the other hand, lower mass flow rates produce a stronger cooling of the HTF. For the MDM case, a Dowtherm-A mass flow rate of about 0.62 kg/s allows the HTF to cool from 350 °C to approximately 270 °C, which corresponds to the desired temperature difference.

The resulting Aspen Plus model is shown in Figure 3.13a. Under these conditions, MDM enters the evaporator as a pressurized liquid at about 157.4 °C and leaves the component in vapor phase at 250 °C, corresponding to the turbine inlet conditions selected in section 3.2.1. At the same time, Dowtherm-A remains in liquid phase and provides the thermal power required for the evaporation process.



(a) Aspen Plus scheme **(b)** Sensitivity analysis

Figure 3.13: MDM - Evaporator modeling and sensitivity analysis in Aspen Plus

Figure 3.14 shows the temperature profiles of Dowtherm-A and MDM inside the evaporator. Dowtherm-A enters the heat exchanger at 350 °C and is cooled down to about 270 °C while transferring heat to the ORC working fluid. On the cold side, MDM first increases its temperature from the pump outlet condition up to the evaporation temperature.
As heat continues to be transferred from Dowtherm-A to the working fluid, the energy supplied is no longer used mainly to increase the temperature, but to

complete the phase change. This evaporation process takes place at nearly constant temperature, until the fluid reaches the vapor state required at the turbine inlet.

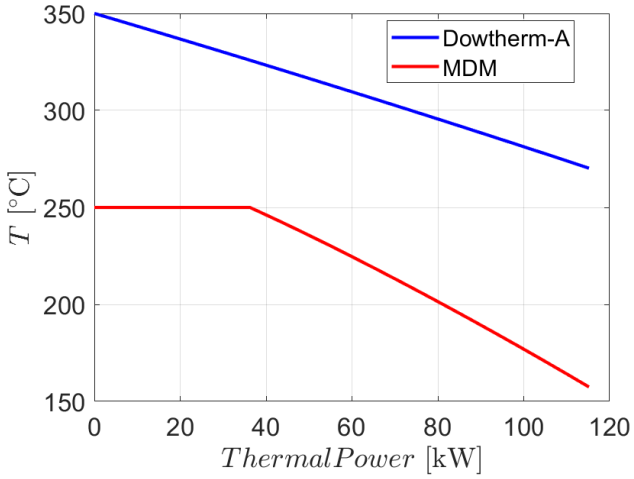
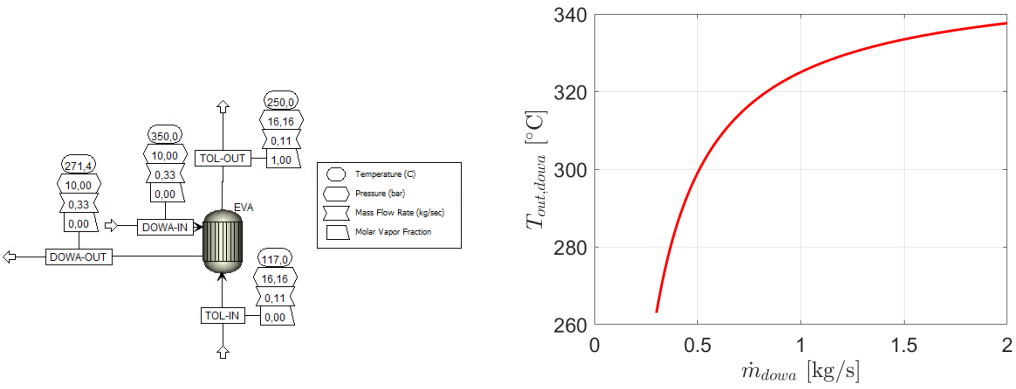


Figure 3.14: MDM - Temperature profiles in the evaporator

The same procedure was applied to Toluene. From the sensitivity analysis, a Dowtherm-A mass flow rate of about 0.33 kg/s was selected, which gives an outlet temperature close to 271 °C. This corresponds to a temperature decrease of approximately 80 °C, in line with the criterion adopted for the evaporator.



(a) Aspen Plus scheme **(b)** Sensitivity analysis

Figure 3.15: Toluene - Evaporator modeling and sensitivity analysis in Aspen Plus

Compared with MDM, the required Dowtherm-A mass flow rate is lower. This is mainly related to the lower mass flow rate of Toluene in the ORC, which reduces

the thermal power required in the evaporator to bring the working fluid to the turbine inlet conditions.

Figure 3.16 reports the T–Q diagram of the evaporator for Toluene. The profile follows the same behavior observed for MDM: the working fluid is first heated up to the evaporation temperature and then changes phase at nearly constant temperature. In this case, the exchanged thermal power is lower, due to the lower Toluene mass flow rate in the ORC.

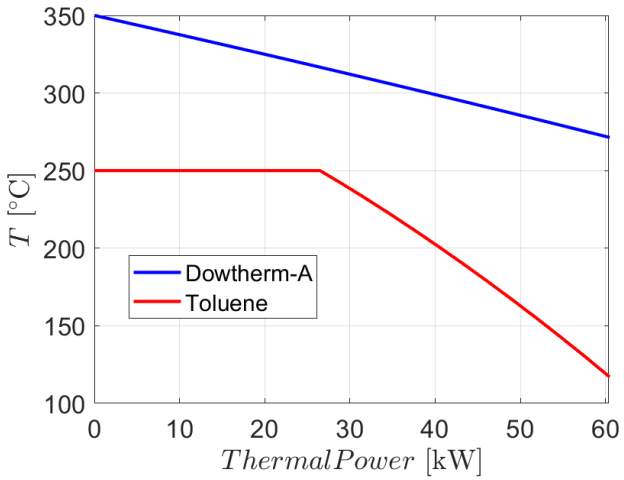


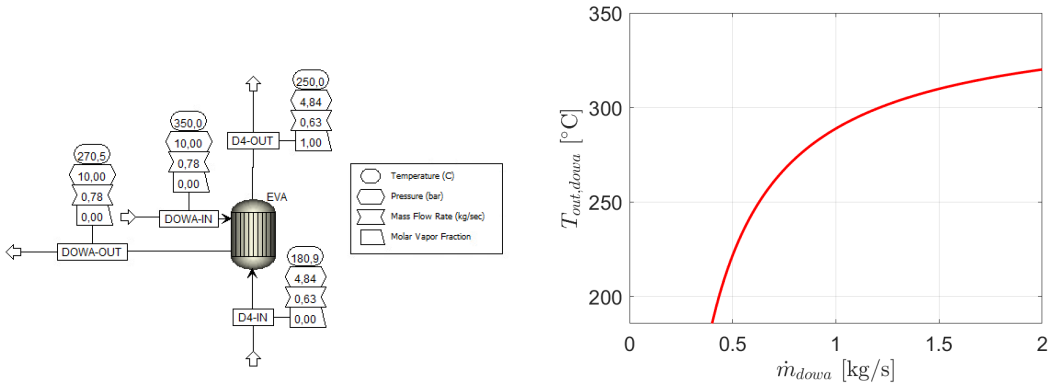
Figure 3.16: Toluene - Temperature profiles in the evaporator

Finally, the same evaporator analysis was carried out for D4. Since the turbine inlet temperature was fixed at 250 °C for all the working fluids, the Dowtherm-A inlet temperature was also kept equal to 350 °C. This choice allowed the three fluids to be compared under the same thermal conditions on the hot side of the evaporator, while keeping the same criterion adopted for the previous cases.

The sensitivity analysis provided a Dowtherm-A mass flow rate of about 0.78 kg/s, which is the highest value among the three fluids. This result is consistent with the higher D4 mass flow rate circulating in the ORC loop. As a consequence, a larger amount of heat has to be transferred in the evaporator in order to bring the working fluid from the pump outlet conditions to the selected turbine inlet state.

Under these conditions, D4 enters the evaporator at about 180.9 °C and leaves it at 250 °C, with a vapor fraction equal to one. This means that the heat supplied by Dowtherm-A is sufficient to complete the evaporation process and to obtain the vapor state required before the expansion phase.

The final evaporator results for D4 are shown in Figure 3.17.



(a) Aspen Plus scheme **(b)** Sensitivity analysis

Figure 3.17: D4 - Evaporator modeling and sensitivity analysis in Aspen Plus

Once the HTF mass flow rate was selected, the T–Q diagram was used as a final check of the heat exchange process for the D4 case. This graph shows how the temperatures of the hot and cold streams vary along the evaporator and helps to verify that the chosen operating conditions are appropriate.

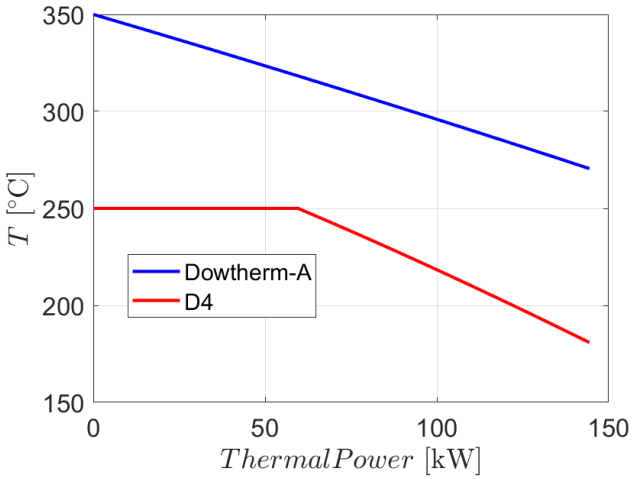


Figure 3.18: D4 - Temperature profiles in the evaporator

The main data used to set up the evaporator model are reported in Table 3.7. These values include the working fluid conditions on the ORC side and the main operating assumptions adopted for Dowtherm-A on the hot side.

	MDM	**Toluene**	**D4**
Inlet temperature $T_{\text{wf,in}}$	157.4 °C	117.0 °C	180.9 °C
Outlet temperature $T_{\text{wf,out}}$	250.0 °C	250.0 °C	250.0 °C
Working fluid mass flow rate $\dot{m}_{wf}$	0.39 kg/s	0.11 kg/s	0.63 kg/s
Evaporator pressure P_{evap}	7.72 bar	16.16 bar	4.84 bar
Dow-A inlet temperature $T_{\text{HTF,in}}$	350.0 °C	350.0 °C	350.0 °C
Dow-A pressure P_{HTF}	10.00 bar	10.00 bar	10.00 bar

Table 3.7: Evaporator modeling assumptions

Table 3.8 reports the main results obtained from the evaporator sensitivity analysis. Starting from an inlet temperature of 350 °C, the outlet temperature remains close to 270 °C in all three cases, showing that the same design criterion was respected.

The heat duty varies from one fluid to another because the amount of thermal energy required in the evaporator depends on the working fluid flow rate and on the thermodynamic path followed before reaching the turbine inlet conditions. In particular, Toluene requires a lower thermal input, while D4 requires the higher one.

	MDM	**Toluene**	**D4**
Dow-A mass flow rate $\dot{m}_{\text{HTF}}$	0.62 kg/s	0.33 kg/s	0.78 kg/s
Heat duty Qeva	115.19 kWth	60.48 kWth	144.40 kWth
Dow-A outlet temperature $T_{\text{HTF,out}}$	270.2 °C	271.4 °C	270.5 °C

Table 3.8: Evaporator sensitivity analysis results

3.3 Base ORC Model

Once the individual components of the ORC system had been modeled, they were assembled to obtain the complete cycle. This allowed the interaction between the different sections of the plant to be evaluated and the overall thermodynamic behavior of the system to be represented. The complete cycle is also shown by means of the corresponding T-s diagram, which highlights the main transformations undergone by the working fluid throughout the process.

3.3.1 MDM Base ORC Configuration

Figures 3.19 and 3.20 show the complete base ORC configuration modeled in Aspen Plus and the corresponding T-s diagram for MDM. In the flowsheet, the four main components of the cycle are connected together: the pump, the evaporator, the turbine and the condenser. The working fluid is pressurized by the pump, heated in the evaporator by the Dowtherm-A stream, expanded in the turbine to produce mechanical power, and finally condensed before returning to the pump inlet. The values reported in the Aspen layout make it possible to follow the main operating conditions at each point of the cycle.

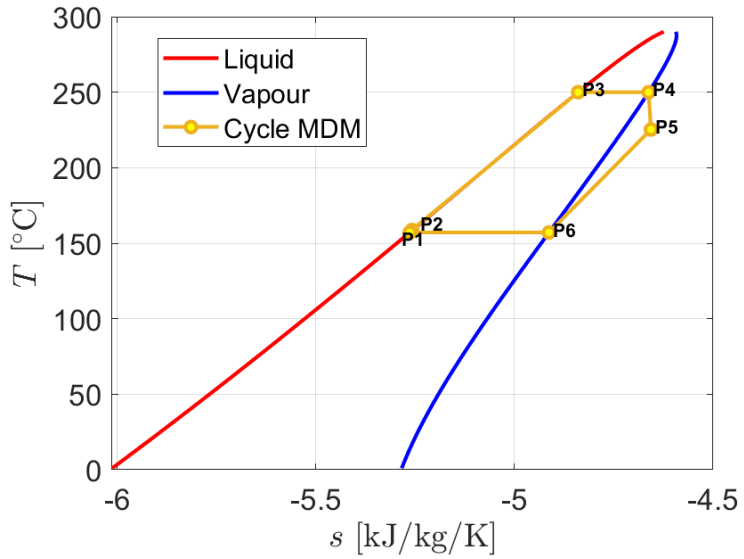


Figure 3.19: T-s diagram of the base ORC cycle using MDM

The T-s diagram provides a complementary view of the same process, highlighting the thermodynamic path followed by the working fluid. It shows the heating and evaporation phase up to the turbine inlet condition, the expansion process, and

the subsequent cooling and condensation stage. In this way, the diagram helps to visualize more clearly how the complete cycle develops with respect to the saturation curves of MDM.

The main transformations represented in the diagram can be summarized as follows:

- **P1–P2:** pressurization of the liquid working fluid through the pump. Since MDM is in the liquid phase, the temperature and entropy variations are very small.
- **P2–P3:** preheating of MDM in the evaporator. In this section, the working fluid receives heat from the Dowtherm-A stream and its temperature increases up to the evaporation region.
- **P3–P4:** evaporation at the high-pressure level. The working fluid reaches the turbine inlet condition, with a temperature of about 250 °C.
- **P4–P5:** expansion through the turbine. During this process, MDM produces mechanical power, while both pressure and temperature decrease.
- **P5–P6:** cooling of the turbine outlet stream in the condenser, before the main condensation phase. The working fluid rejects heat to the water stream.
- **P6–P1:** condensation at the low-pressure level. MDM returns to the liquid state and is then sent back to the pump, closing the cycle.

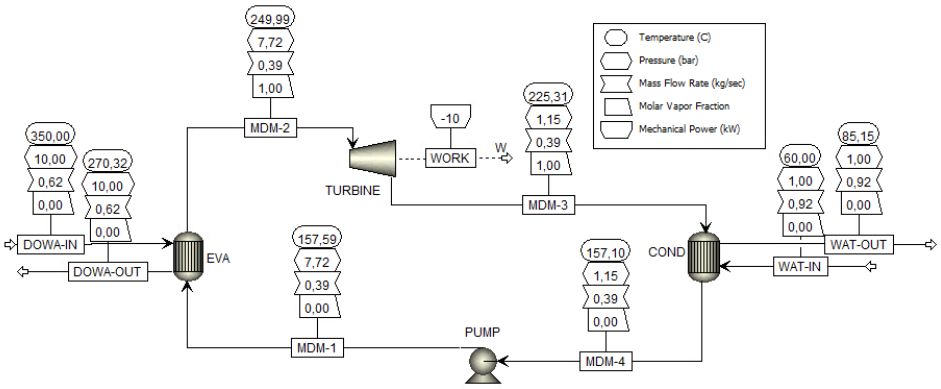


Figure 3.20: Aspen Plus layout of the MDM-based ORC system

3.3.2 Toluene Base ORC Configuration

After the analysis of the MDM case, the same base ORC configuration was simulated using Toluene as working fluid. The general layout of the plant remains unchanged, since the cycle is still composed of the pump, evaporator, turbine and condenser. However, due to the different thermodynamic properties of Toluene, the operating conditions are noticeably different from those obtained with MDM.

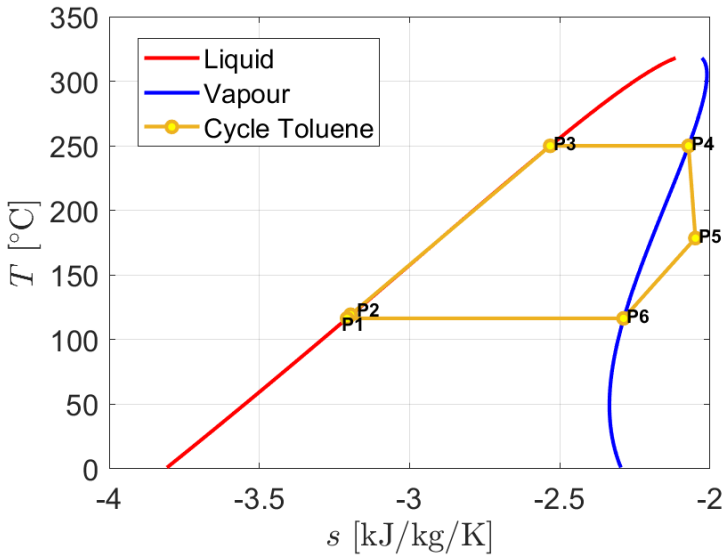


Figure 3.21: T-s diagram of the base ORC cycle using Toluene

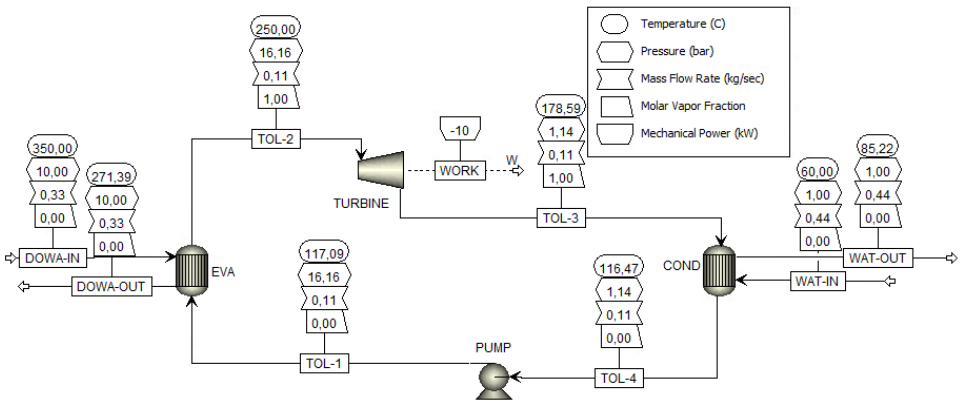


Figure 3.22: Aspen Plus layout of the Toluene-based ORC system

Figures 3.21 and 3.22 report the thermodynamic cycle and the Aspen Plus flowsheet obtained for the Toluene case. Compared with MDM, the most relevant differences concern the pressure levels and the circulating mass flow rate. In particular, Toluene requires a higher evaporation pressure to reach the selected turbine inlet temperature of 250 °C, while a lower mass flow rate is sufficient to obtain the target mechanical power output. This behavior is also reflected in the T-s diagram, where the cycle appears more compact, especially along the entropy axis.

3.3.3 D4 Base ORC Configuration

The last working fluid considered for the base ORC configuration is D4. As for the previous cases, the same plant layout was maintained, in order to compare the three fluids under a consistent cycle arrangement.

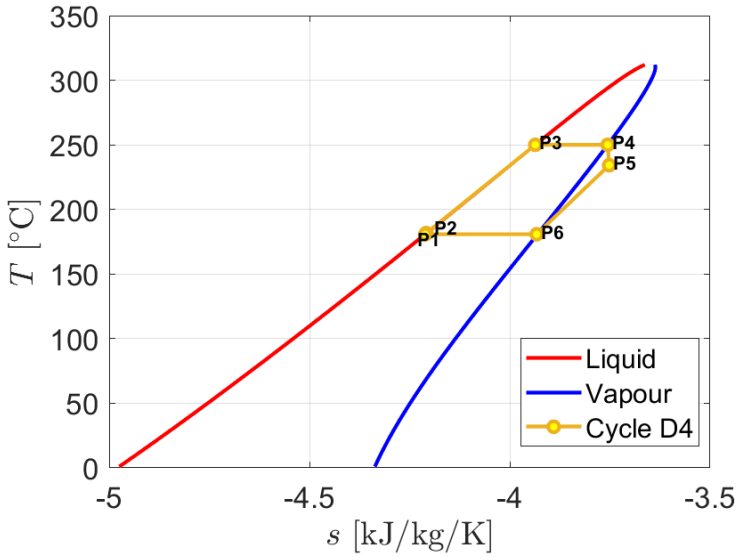


Figure 3.23: T-s diagram of the base ORC cycle using D4

Figures 3.23 and 3.24 show the base ORC cycle obtained with D4 as working fluid. Compared with MDM and Toluene, D4 operates at a lower evaporation pressure, while requiring a higher circulating mass flow rate to achieve the same mechanical power output. This can be seen from the Aspen Plus flowsheet, where the mass flow rate is the highest among the three fluids.

From the T-s diagram, the cycle develops at a higher condensation temperature level, while keeping the same general sequence of heating, expansion, cooling and condensation already observed in the previous cases.

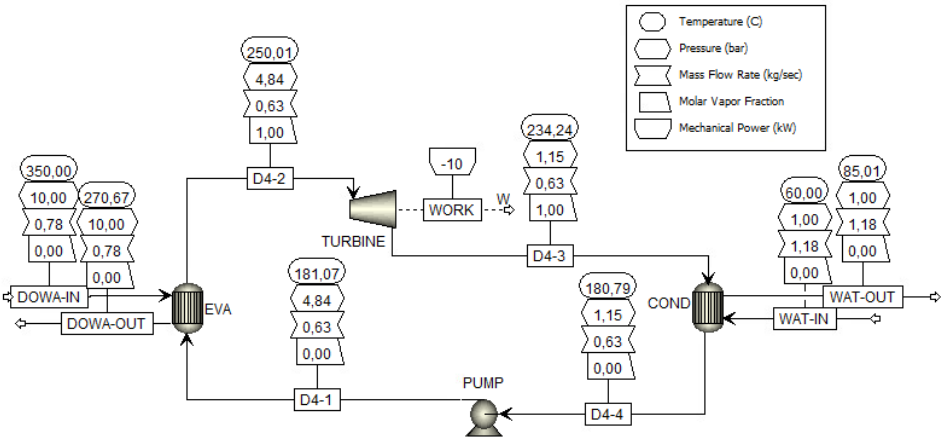


Figure 3.24: Aspen Plus layout of the D4-based ORC system

3.4 Regenerative ORC Model

After the base ORC configuration had been analyzed for the selected working fluids, a regenerative layout was considered as a possible improvement of the cycle. The aim of this modification is to recover part of the thermal energy still available after the first expansion stage and use it to preheat the working fluid before entering the evaporator.

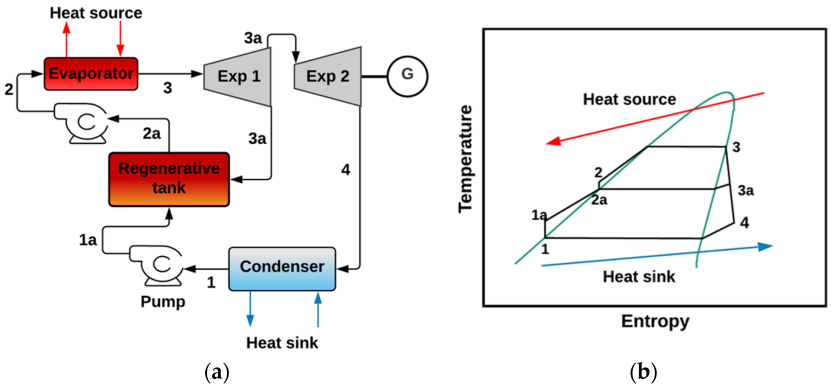


Figure 3.25: Regenerative ORC scheme and T-s diagram [10]

In this way, the external heat required by the cycle can be reduced, potentially improving the overall thermodynamic performance of the system. The regenerative configuration adopted in this work is shown in Figure 3.25.

3.4.1 MDM Regenerative ORC Configuration

The regenerative configuration was implemented in Aspen Plus starting from the base ORC model previously developed for MDM. The main modification consists in dividing the expansion process into two turbine stages, with an intermediate extraction of part of the working fluid. To model this layout, a second turbine block was added, together with a splitter and a mixer. The splitter and mixer were selected from the *Mixers/Splitters* library in Aspen Plus.

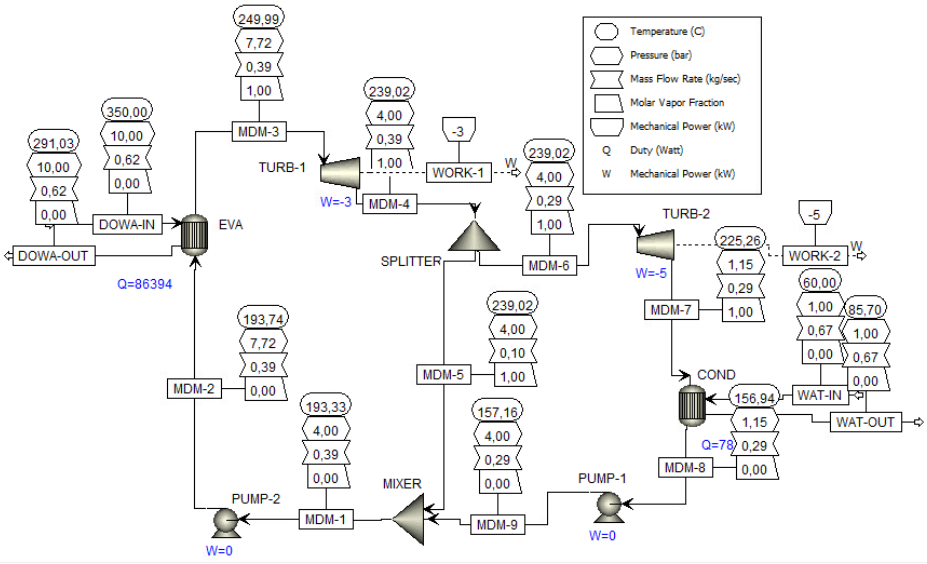


Figure 3.26: Aspen Plus layout of the MDM-based regenerative ORC system

After the first expansion stage, a fraction of the vapor stream is extracted and sent to the mixer, where it is combined with the liquid stream coming from the condenser and the first pump. This mixing process increases the temperature of the working fluid before it enters the evaporator, reducing the thermal duty required from the external heat source.

Particular attention was paid to the state of the stream entering the second pump, since the pump must operate with a completely liquid fluid. For this reason, the molar vapor fraction at the pump inlet was checked to ensure that no vapor phase was present before pressurizing the fluid up to the evaporation pressure.

In the regenerative configuration, the cooling water mass flow rate was adjusted in order to keep the outlet temperature close to 85 °C, as in the base cycle. Compared with the original MDM configuration, the required water flow rate decreases from 0.92 kg/s to 0.67 kg/s. This reduction is mainly due to the intermediate extraction of part of the working fluid after the first turbine stage: only the remaining flow continues through the second turbine and reaches the condenser. As a result, the heat rejected in the condenser is lower than in the base cycle, and a smaller water flow rate is sufficient to achieve the same water temperature rise from 60 °C to about 85 °C.

After defining the regenerative layout, a sensitivity analysis was carried out to identify the most suitable bleeding conditions for the cycle. Two parameters were varied: the bleeding pressure and the bleeding mass flow rate. For each combination, the electric efficiency and the overall plant efficiency were evaluated, in order to understand how the choice of the extraction point affects the performance of the system.

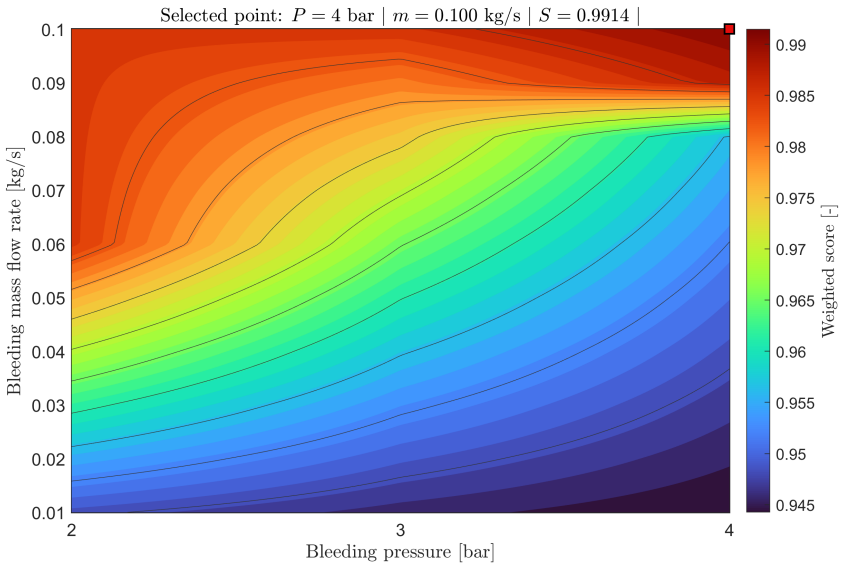


Figure 3.27: MDM - bleeding sensitivity analysis

Since the two efficiencies do not necessarily reach their maximum value under the same operating conditions, a weighted score was introduced to select a balanced operating point.

Both efficiencies were first normalized with respect to the maximum value obtained within the analyzed range, and the same weight was assigned to each contribution:

$$S = 0.5\frac{\eta_{\text{el}}}{\eta_{\text{el,max}}} + 0.5\frac{\eta_{\text{plant}}}{\eta_{\text{plant,max}}} \tag{3.1}$$

where S is the weighted score, η_{el} is the electric efficiency and η_{plant} is the overall plant efficiency.

The resulting score was then represented as a function of the bleeding pressure and bleeding mass flow rate, as shown in Figure 3.27. In this way, the operating region providing the best compromise between electric efficiency and overall plant efficiency can be identified more clearly.

Only the simulations that successfully converged and provided a completely liquid stream at the pump inlet were considered valid. The selected point was then identified as the combination of bleeding pressure and bleeding mass flow rate that maximized the weighted score within the investigated range. For MDM, this condition corresponds to a bleeding pressure of 4 bar and a bleeding mass flow rate of 0.100 kg/s.

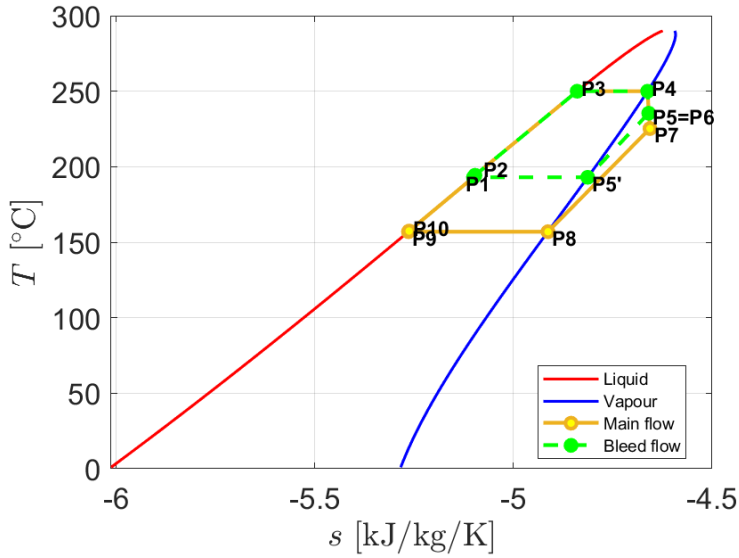


Figure 3.28: T-s diagram of the regenerative ORC cycle using MDM

The main transformations represented in the T-s diagram of the regenerative cycle can be summarized as follows:

- **P1–P2:** pressurization through the second pump, which brings the working fluid from the intermediate pressure to the evaporation pressure before entering the evaporator.
- **P2–P3:** preheating of the working fluid in the evaporator. In this section, the fluid receives heat from the Dowtherm-A stream and its temperature increases up to the evaporation region.
- **P3–P4:** evaporation at the high-pressure level. The working fluid reaches the inlet condition of the first turbine stage, with a temperature of about 250 °C.
- **P4–P5/P6:** first expansion stage. The working fluid expands from the evaporation pressure to the intermediate bleeding pressure.
- **P5–P5':** path of the extracted fraction towards the mixer. This line represents the bled stream used for the regenerative mixing process.
- **P6–P7:** second expansion stage, where the main flow expands down to the condenser pressure.
- **P7–P8:** cooling of the turbine outlet stream in the condenser, before the main condensation phase.
- **P8–P9:** condensation at the low-pressure level. The working fluid rejects heat to the water stream and returns to the liquid state, closing the cycle.
- **P9–P10:** pressurization of the liquid working fluid through the first pump, from the condenser pressure to the intermediate bleeding pressure.
- **P10 + P5' → P1:** mixing process between the liquid stream coming from the first pump and the extracted stream from the first turbine stage. The resulting stream leaves the mixer at point P1.

The results obtained for the regenerative MDM configuration show a clear reduction in both the evaporator and condenser heat duties compared with the base cycle. In particular, the evaporator duty decreases from 115.19 kWth to 86.39 kWth, while the condenser duty decreases from 105.42 kWth to 78.36 kWth. This is a direct consequence of the regenerative layout, where part of the working fluid is extracted after the first turbine stage and used to preheat the liquid stream before entering the evaporator. As a result, less external heat is required from the Dowtherm-A stream and less heat has to be rejected in the condenser. However, the introduction of bleeding also reduces the mass flow rate that expands through the second turbine stage. For this reason, the total mechanical power produced by the two turbines is lower than in the base configuration and no longer reaches the original target

of 10 kW. In the regenerative case, the turbine power output is about 8.27 kW before subtracting the pump consumption. This reduction represents the main trade-off of the regenerative solution: the cycle requires less thermal input, but it also produces a lower power output.

Parameter	**MDM regenerative cycle**
Evaporator heat duty Q_{eva}	86.39 kWth
Condenser heat duty Q_{cond}	78.36 kWth
Cooling water mass flow rate $\dot{m}_{\text{water}}$	0.67 kg/s
First turbine mechanical power $W_{\text{turb,1}}$	3.14 kW
Second turbine mechanical power $W_{\text{turb,2}}$	5.13 kW
First pump power consumption $W_{\text{pump,1}}$	0.14 kW
Second pump power consumption $W_{\text{pump,2}}$	0.26 kW
Evaporator inlet temperature $T_{\text{eva,in}}$	193.74 °C
Bleeding mass flow rate $\dot{m}_{\text{bleed}}$	0.10 kg/s
Bleeding pressure p_{bleed}	4.00 bar

Table 3.9: Main results of the MDM regenerative ORC cycle

3.4.2 Toluene Regenerative ORC Configuration

The same regenerative layout adopted for MDM was then applied to Toluene, keeping the same sensitivity procedure to select the bleeding conditions.

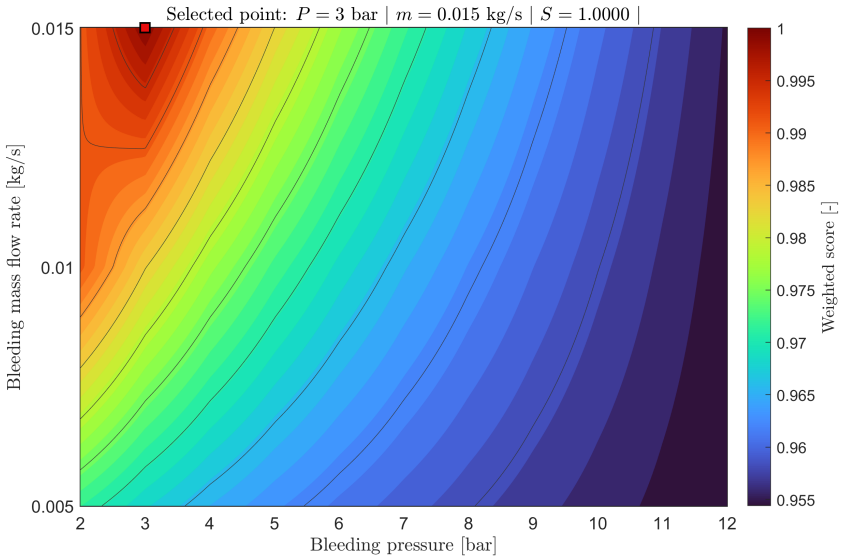


Figure 3.29: Toluene bleeding sensitivity analysis

As shown in Figure 3.29, the maximum value of the weighted score is obtained for a bleeding pressure of 3 bar and a bleeding mass flow rate of 0.015 kg/s. This operating point was therefore selected for the regenerative Toluene cycle, as it provides the best compromise between electric efficiency and overall plant efficiency within the analyzed range.

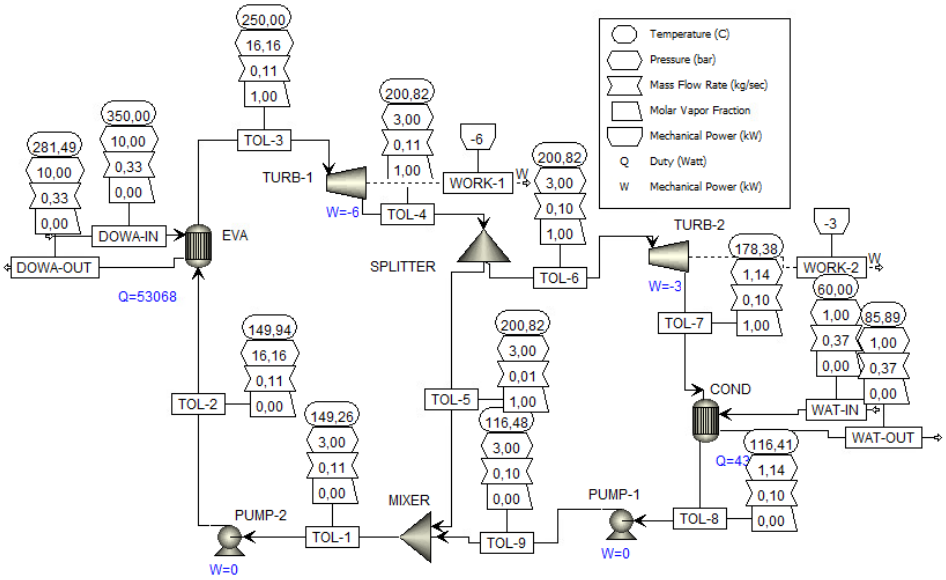


Figure 3.30: Aspen Plus layout of the Toluene-based regenerative ORC system

The Aspen Plus layout was then obtained by applying the selected bleeding conditions to the regenerative cycle. As in the MDM case, the expansion is divided into two turbine stages, with an intermediate extraction between them. For Toluene, the extracted mass flow rate is significantly lower, consistently with the lower circulating flow rate required by this fluid.

The T-s diagram was used as a final check of the operating point selected from the sensitivity analysis. The state points are correctly positioned with respect to the saturation region, and the main sections of the regenerative cycle are clearly identifiable. The selected bleeding conditions therefore provide a consistent cycle representation, both during expansion and during condensation.
In particular, the diagram confirms that the working fluid reaches the liquid region before being pressurized again, which is an essential requirement for the correct operation of the pumps.

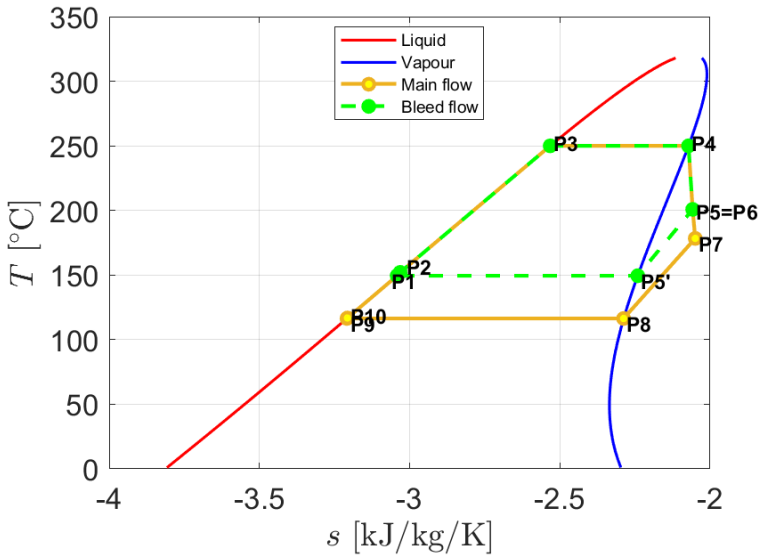


Figure 3.31: T-s diagram of the regenerative ORC cycle using Toluene

The results obtained for the regenerative Toluene cycle show that the selected bleeding conditions lead to a weighted score equal to 1. This means that, within the analyzed range, the maximum electric efficiency and the maximum overall plant efficiency are reached at the same operating point. Therefore, unlike the MDM case, no relevant compromise between the two efficiencies is required. The selected condition corresponds to a bleeding pressure of 3 bar and a bleeding mass flow rate of 0.015 kg/s, which is then used for the final regenerative configuration.

Parameter	**Toluene regenerative cycle**
Evaporator heat duty Q_{eva}	53.07 kWth
Condenser heat duty Q_{cond}	43.59 kWth
Cooling water mass flow rate $\dot{m}_{\text{water}}$	0.37 kg/s
First turbine mechanical power $W_{\text{turb,1}}$	6.28 kW
Second turbine mechanical power $W_{\text{turb,2}}$	3.25 kW
First pump power consumption $W_{\text{pump,1}}$	0.025 kW
Second pump power consumption $W_{\text{pump,2}}$	0.218 kW
Evaporator inlet temperature $T_{\text{eva,in}}$	149.94 °C
Bleeding mass flow rate $\dot{m}_{\text{bleed}}$	0.015 kg/s
Bleeding pressure p_{bleed}	3.00 bar

Table 3.10: Main results of the Toluene regenerative ORC cycle

3.4.3 D4 Regenerative ORC Configuration

The regenerative analysis was finally extended to D4, completing the comparison between the three selected working fluids. In this case, the same optimization criterion was applied, but the sensitivity results identified a different operating region due to the specific thermodynamic behavior of D4.

For D4, the selected point is located at the lowest pressure investigated, equal to 2 bar, with a bleeding mass flow rate of 0.120 kg/s and a weighted score of 0.9947. Although the score does not reach exactly unity, it remains very close to the maximum value, indicating that the selected condition provides a well-balanced compromise between electric efficiency and overall plant efficiency.

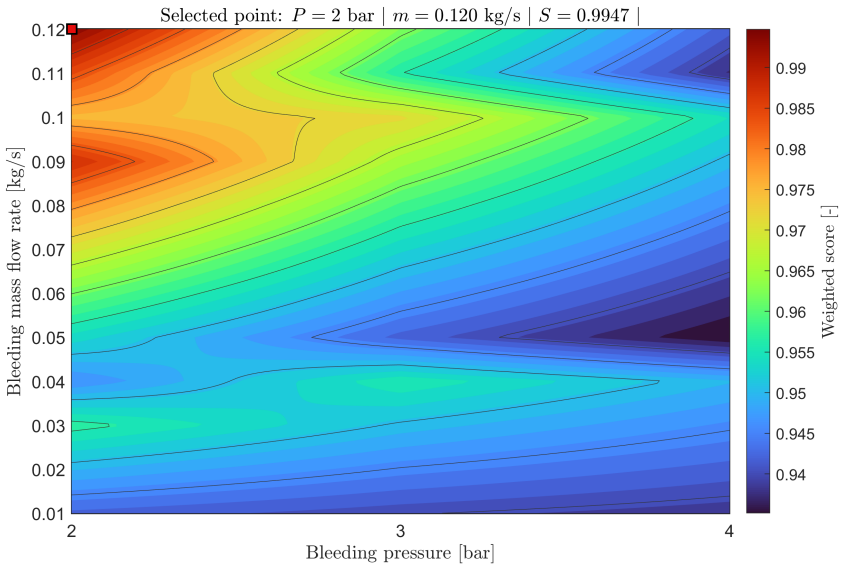


Figure 3.32: D4 bleeding sensitivity analysis

The Aspen Plus model and the T-s diagram were then obtained using the selected bleeding conditions. In this case, the extraction point is located closer to the low-pressure section of the cycle than in the previous fluids, and this affects the position of the regenerative branch in the T-s diagram. The cycle representation remains coherent with the saturation region, while the condenser section is located at a higher temperature level. This confirms that the regenerative configuration can also be applied to D4 without modifying the general structure of the cycle.

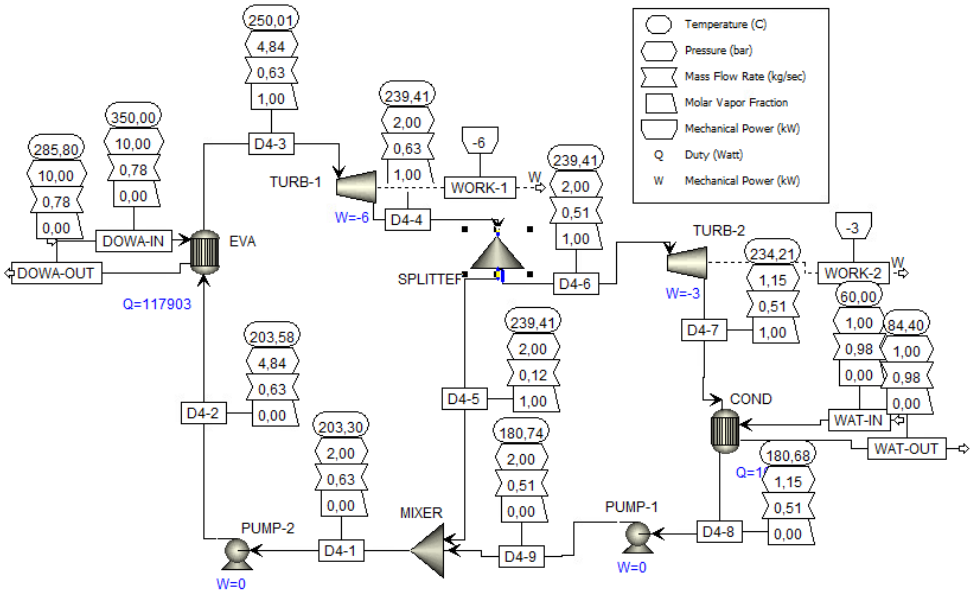


Figure 3.33: Aspen Plus layout of the D4-based regenerative ORC system

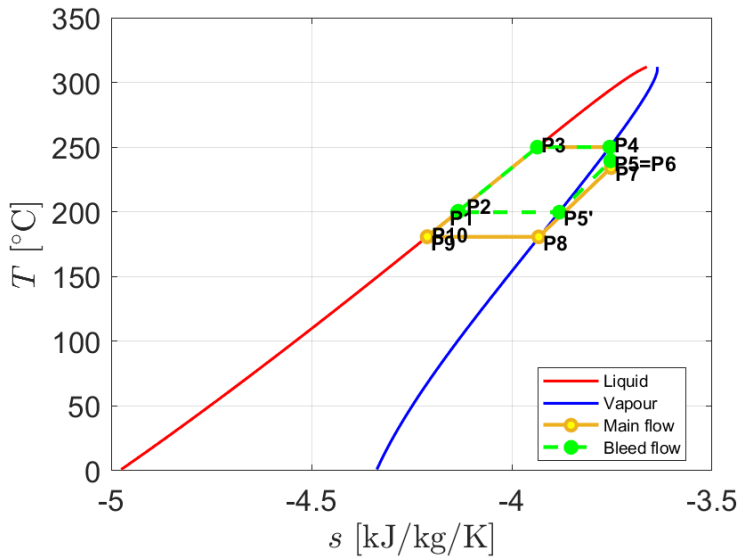


Figure 3.34: T-s diagram of the regenerative ORC cycle using D4

The main results obtained for the regenerative D4 configuration are summarized in Table 3.11. The selected bleeding conditions lead to a reduction in the evaporator heat duty compared with the corresponding base cycle, while the condenser duty remains relatively high due to the thermal level at which the cycle operates. The total turbine power is distributed between the two expansion stages, and the pump consumption remains small compared with the power produced by the turbines. These results provide the reference values used later for the comparison between the base and regenerative configurations.

Parameter	**D4 regenerative cycle**
Evaporator heat duty Q_{eva}	117.90 kWth
Condenser heat duty Q_{cond}	108.80 kWth
Cooling water mass flow rate $\dot{m}_{\text{water}}$	0.98 kg/s
First turbine mechanical power $W_{\text{turb,1}}$	5.97 kW
Second turbine mechanical power $W_{\text{turb,2}}$	3.29 kW
First pump power consumption $W_{\text{pump,1}}$	0.063 kW
Second pump power consumption $W_{\text{pump,2}}$	0.274 kW
Evaporator inlet temperature $T_{\text{eva,in}}$	195.82 °C
Bleeding mass flow rate $\dot{m}_{\text{bleed}}$	0.120 kg/s
Bleeding pressure p_{bleed}	2.00 bar

Table 3.11: Main results of the D4 regenerative ORC cycle

Chapter 4

Solar Field Modeling and ORC Performance

In this chapter, the ORC system previously modeled is coupled with the solar field in order to evaluate the overall behavior of the plant under solar-driven operation. The thermal power required by the evaporator is used as the reference value for the solar field sizing, considering both the base and regenerative configurations for the three selected working fluids. The analysis first focuses on the definition of the main solar field parameters and efficiencies, and then on the estimation of the number of collectors required to supply the heat demand of each cycle. In this way, the different ORC configurations can be compared not only in terms of thermodynamic performance, but also from the point of view of the solar field size needed for their operation.

4.1 Solar Field Operating Conditions

Before sizing the solar field, an operating threshold was introduced in order to estimate the time interval during which the solar concentrator can effectively supply heat to the ORC system. In this work, the reference value was set equal to 350 °C, corresponding to the inlet temperature assumed for the Dowtherm-A stream entering the evaporator.
It should be noted that this value is used as a simplified criterion. The temperature reached at the focus of the paraboloid does not directly coincide with the actual temperature of the heat transfer fluid, since the latter also depends on the receiver design, heat transfer process and thermal losses.

However, comparing the seasonal focal temperature profiles with the 350 °C threshold provides a useful preliminary indication of the daily operating window of the solar-driven cycle.

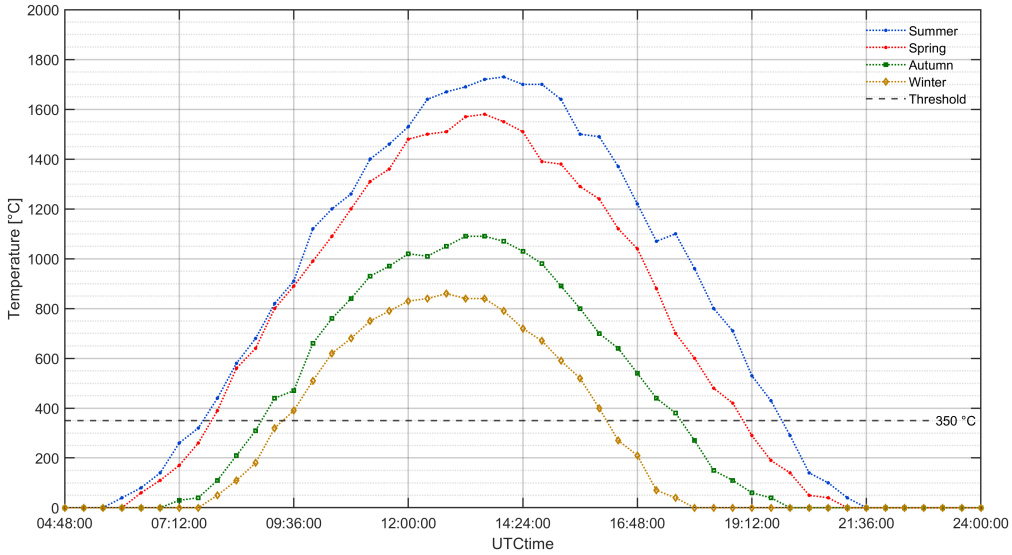


Figure 4.1: Seasonal focal temperature profiles with operating threshold

As shown in Figure 4.1, the 350 °C threshold is exceeded for a different number of hours depending on the season. Longer operating windows are obtained during spring and summer, while autumn and winter show a more limited availability. These time intervals are then used to estimate the annual operating hours of the solar-driven ORC system.

Season	**Operating time slot**	**Operating hours**
Spring	7:55–19:00	11 h 05 min
Summer	7:40–19:45	12 h 05 min
Autumn	9:00–17:40	8 h 40 min
Winter	9:20–16:10	6 h 50 min

Table 4.1: Seasonal operating hours of the solar-driven ORC system

Based on the intersection between the seasonal focal temperature profiles and the 350 °C threshold, the operating time slot of the solar-driven ORC system was estimated for each season. The resulting operating windows and the corresponding daily operating hours are reported in Table 4.1.

After defining the seasonal operating windows, representative clear-sky days were selected for each season in order to estimate the corresponding direct normal irradiance. The DNI values used in the solar field sizing are reported in Table 4.2.

Season	**Selected day**	**DNI [W/m^2]**
Spring	30 May	857.87
Summer	29 July	786.10
Autumn	4 November	605.46
Winter	14 December	701.17

Table 4.2: Seasonal direct normal irradiance values for the selected reference days

The operating intervals previously identified were then converted into daily operating minutes. These values were multiplied by the number of days of each season in order to estimate the seasonal operating time of the solar-driven ORC system. The resulting values are reported in Table 4.3.

Season	**Daily operating time [min]**	**Seasonal operating time [min]**
Spring	665	61845
Summer	725	67425
Autumn	520	46800
Winter	410	36490

Table 4.3: Daily and seasonal operating time

Starting from the seasonal operating times, the equivalent annual operating hours of the solar-driven ORC system were calculated. In addition, the annual average DNI was obtained from the seasonal reference values previously reported.

Parameter	**Value**
Annual operating hours	3542.67 h
Annual average DNI	752.63 W/m^2

Table 4.4: Annual operating hours and direct normal irradiance

4.2 Solar Field Sizing

The first step in the solar field sizing is to identify the thermal load that has to be supplied to the evaporator. This value depends on both the selected working fluid and the cycle configuration. For this reason, the evaporator heat duties obtained for the base and regenerative layouts are reported together in Table 4.5.

Configuration	**MDM**	**Toluene**	**D4**
Base cycle – Q_{eva}	115.19 kWth	60.48 kWth	144.40 kWth
Regenerative cycle – Q_{eva}	86.39 kWth	53.07 kWth	117.90 kWth

Table 4.5: Evaporator thermal load for the analyzed ORC configuration

After defining the thermal power required by the evaporator, the next step is to estimate the useful thermal power that can be supplied by a single solar collector. The main data used for this calculation are the aperture area of the parabolic dish, the optical efficiency of the reflective surface and the annual average DNI previously obtained. These values are used only as sizing parameters, since the geometry and operating principle of the concentrator have already been described in the previous chapter.

$$Q_{\text{csp}} = DNI_{\text{annual}} \cdot \eta_{\text{opt}} \cdot A_{\text{dish}} \tag{4.1}$$

Parameter	**Value**
Annual average DNI	752.63 W/m^2
Optical efficiency η_{opt}	0.80
Dish aperture area A_{dish}	4.5 m^2
Thermal power per collector Q_{csp}	2.71 kW$_{\text{th}}$

Table 4.6: Useful thermal power provided by a single solar collector

Once the useful thermal power provided by a single collector has been estimated, the number of parabolic dishes required for each configuration can be calculated. The sizing is based on the evaporator thermal load reported previously, since the solar field has to supply the heat required by the working fluid during the evaporation process.

$$N_{\text{coll}} = \frac{Q_{\text{eva}}}{Q_{\text{csp}}} \tag{4.2}$$

where N_{coll} is the number of collectors, Q_{eva} is the evaporator heat duty of the considered cycle configuration and Q_{csp} is the useful thermal power provided by a single parabolic dish collector.

Since the number of collectors must be an integer, the values obtained from the ratio were rounded up to the nearest whole number. This ensures that the installed solar field is able to cover the required evaporator thermal load for each working fluid and cycle configuration.

Configuration	**MDM**	**Toluene**	**D4**
Base cycle – N_{coll}	43	23	54
Regenerative cycle – N_{coll}	32	20	44

Table 4.7: Required number of parabolic dish collectors

As shown in Table 4.7, the number of collectors is strongly influenced by the evaporator heat duty of each configuration. Toluene requires the lowest number of collectors in both the base and regenerative cycles, while D4 requires the largest solar field. For all the working fluids, the regenerative configuration reduces the required number of collectors, since part of the heat demand is internally recovered within the cycle.

Besides the number of collectors, the solar field can also be described in terms of total aperture area. This value is useful because it gives a direct indication of the overall surface required to supply the evaporator heat demand, without referring only to the rounded number of installed collectors.
For each working fluid and cycle configuration, the required area was calculated from the evaporator thermal load and the useful solar power available per unit aperture area:

$$A_{\text{solar,field}} = \frac{Q_{\text{eva}}}{DNI_{\text{annual}} \cdot \eta_{\text{opt}}} \tag{4.3}$$

Configuration	**MDM**	**Toluene**	**D4**
Base cycle – $A_{\text{solar,field}}$	191.31 m^2	100.45 m^2	239.82 m^2
Regenerative cycle – $A_{\text{solar,field}}$	143.48 m^2	88.14 m^2	195.82 m^2

Table 4.8: Required solar field aperture area

4.3 Configuration Comparison

After the solar field sizing, the results obtained for the base and regenerative configurations can be discussed together. The previous tables showed that regeneration reduces both the evaporator heat duty and the required solar field size for all the selected working fluids. This effect is particularly relevant because the evaporator load is the parameter that directly determines the number of collectors and the total aperture area required by the plant.

However, the reduction in solar field size must be evaluated together with the thermodynamic performance of the cycle. For this reason, the comparison is completed by considering the electric efficiency and the overall plant efficiency for each working fluid and configuration.

The comparison was then completed by evaluating the main efficiency indicators of the cycle. In this case, the electric power output was considered rather than the mechanical power produced by the turbine. The turbine mechanical power represents the shaft power before the conversion into electricity, while the electric power also accounts for the mechanical and generator efficiencies. Therefore, the net electric power of the cycle was calculated by subtracting the electric consumption of the pump, or pumps in the regenerative configuration, from the gross electric power produced by the generator.

For the base cycle, the net electric power is calculated as:

$$W_{\mathrm{el,net,b}} = W_{\mathrm{el,turb}} - W_{\mathrm{el,pump}} \tag{4.4}$$

while for the regenerative cycle, where two turbine stages and two pumps are present, it becomes:

$$W_{\mathrm{el,net,r}} = W_{\mathrm{el,turb,1}} + W_{\mathrm{el,turb,2}} - W_{\mathrm{el,pump,1}} - W_{\mathrm{el,pump,2}} \tag{4.5}$$

The solar power incident on the installed collector field is given by:

$$Q_{\mathrm{solar}} = N_{\mathrm{coll}} \cdot A_{\mathrm{dish}} \cdot DNI_{\mathrm{annual}} \tag{4.6}$$

The electric efficiency is then defined as:

$$\eta_{\mathrm{el}} = \frac{W_{\mathrm{el,net}}}{Q_{\mathrm{solar}}} \tag{4.7}$$

The overall plant efficiency is calculated by also considering the thermal power rejected at the condenser, which can potentially be recovered as useful heat:

$$\eta_{\text{plant}} = \frac{W_{\text{el,net}} + Q_{\text{cond}}}{Q_{\text{solar}}} \tag{4.8}$$

Finally, the ORC efficiency is evaluated by referring only to the thermal power supplied to the evaporator:

$$\eta_{\text{ORC}} = \frac{W_{\text{el,net}}}{Q_{\text{eva}}} \tag{4.9}$$

These indicators allow the two configurations to be compared from different points of view:

- η_{el} evaluates the electric power production with respect to the solar power incident on the total aperture area of the installed collectors.
- η_{plant} considers both the net electric power and the thermal power rejected at the condenser, giving a more complete indication of the overall useful output of the system.
- η_{ORC} refers only to the thermodynamic cycle and compares the net electric power output with the thermal power supplied to the evaporator.

The resulting efficiency values for the base and regenerative configurations are reported in Table 4.9, allowing a direct comparison between the three working fluids.

Efficiency indicator	**Configuration**	**MDM**	**Toluene**	**D4**
Electric efficiency η_{el}	**Base cycle**	6.44%	12.27%	5.17%
	Regenerative cycle	7.11%	13.43%	5.86%
Plant efficiency η_{plant}	**Base cycle**	78.83%	77.12%	78.67%
	Regenerative cycle	79.41%	77.78%	78.87%
ORC efficiency η_{ORC}	**Base cycle**	8.14%	15.81%	6.55%
	Regenerative cycle	8.92%	17.14%	7.41%

Table 4.9: Efficiency comparison between base and regenerative configurations

The results show that the regenerative configuration leads to higher efficiency values for all the selected working fluids, even though the net electric power output is reduced compared with the corresponding base cycle. This behavior is due to the fact that the regenerative layout significantly decreases the external heat required by the evaporator and, consequently, the solar field size needed to supply the cycle.

Therefore, the reduction in the energy input is more relevant than the decrease in electric production.
The increase in ORC efficiency is mainly related to the lower evaporator heat duty, while the improvement in electric efficiency is associated with the lower solar power incident on the reduced collector field. The variation in the overall plant efficiency is less pronounced, since this indicator also includes the thermal power rejected at the condenser, which is lower in the regenerative configuration.

Among the three working fluids, Toluene represents the most balanced solution. Although MDM and D4 show slightly higher overall plant efficiency values, this is mainly related to the larger amount of heat available at the condenser.
From the point of view of electric production and solar field sizing, Toluene provides the best compromise, since it combines the highest electric and ORC efficiencies with the lowest evaporator heat duty, the smallest required solar field area and the lowest number of collectors.
For this reason, Toluene can be considered the most suitable working fluid among those analyzed in this work, especially when both thermodynamic performance and solar field requirements are taken into account.

Chapter 5

Economic Assessment of the Plant

After the thermodynamic analysis and the comparison between the selected working fluids, an economic assessment is needed to evaluate the feasibility of the proposed plant from a broader perspective. The choice of the best configuration cannot be based only on efficiency, since the investment cost is strongly influenced by the size of the solar field, the number of collectors required and the cost of the main components.

In the previous chapter, toluene was identified as the most suitable working fluid, mainly because it provides a good compromise between cycle performance and solar field size. Starting from this result, the present chapter estimates the investment cost of the plant and evaluates its economic return. The analysis is intended as a preliminary assessment, useful to understand whether the selected technical solution can also be considered reasonable from an economic point of view.

The chapter first describes the methodology adopted for the cost estimation and then applies it to the selected plant layout. Finally, the payback period is calculated in order to assess the time required to recover the initial investment through the useful energy produced by the system.

5.1 Cost Estimation Methodology

The investment cost was estimated according to the methodology proposed by the National Energy Technology Laboratory (NETL) in its Quality Guidelines for Energy System Studies [20]. This approach is commonly used for preliminary techno-economic assessments of power plants and provides a structured procedure

for estimating plant costs on a consistent basis. In particular, it defines different levels of capital cost and allows the contribution of the main plant components to be evaluated separately.
Although the NETL methodology was originally developed for power generation systems, it can also be applied to other energy conversion plants when a preliminary cost assessment is required. For this reason, it was considered suitable for the present study, where the aim is not to obtain a detailed industrial quotation, but to compare the economic impact of the selected plant configuration and estimate the order of magnitude of the investment cost. The resulting capital cost is then used as the basis for the payback period calculation.

In the NETL approach, the investment cost is not evaluated as a single value from the beginning, but is built step by step through five cost levels. Each level adds further contributions to the previous one, starting from the cost of the installed equipment and progressively including engineering activities, indirect costs, owner's costs and the effect of the construction period. The five levels are:

- Bare Erected Cost (BEC);
- Engineering, Procurement and Construction Cost (EPCC);
- Total Plant Cost (TPC);
- Total Overnight Cost (TOC);
- Total As-Spent Cost (TASC).

In the following sections, each cost level is briefly described and then applied to the plant configuration considered in this work.

5.1.1 Estimation of BEC

The first cost level considered in the economic assessment is the Bare Erected Cost (BEC), which includes the purchase cost of the main plant components together with the costs associated with their installation. Since equipment prices depend on size and are not always directly available from manufacturers, a preliminary estimation procedure was adopted.
The purchase cost of each component was evaluated using the correlations proposed by Turton et al. [21]. These correlations relate the equipment cost to a characteristic design parameter, such as the heat transfer area for heat exchangers or the power for rotating equipment, and provide the purchase cost under base conditions, C_p^0.

The base value was then corrected to account for the actual material of construction and operating pressure of the component:

$$C_p = C_p^0 F_M F_P \tag{5.1}$$

where C_p is the corrected purchase cost, F_M is the material correction factor, and F_P is the pressure correction factor.

The purchase cost under base conditions was calculated using the following correlation:

$$\log_{10}\left(C_p^0\right) = K_1 + K_2 \log_{10}(A) + K_3 \left[\log_{10}(A)\right]^2 \tag{5.2}$$

where A is the characteristic size parameter of the equipment, while K_1, K_2 and K_3 are coefficients that depend on the component type. The heat transfer area was used for the heat exchangers, whereas the shaft power was adopted for the pump and the turbine.
The material correction factor, F_M, accounts for the material of construction of the equipment. In the present analysis, the reference material associated with the cost correlations was assumed for all the components, and therefore:

$$F_M = 1 \tag{5.3}$$

The pressure correction factor, F_P, was calculated through the following expression:

$$\log_{10}(F_P) = C_1 + C_2 \log_{10}(P) + C_3 \left[\log_{10}(P)\right]^2 \tag{5.4}$$

where P is the operating pressure expressed as gauge pressure, while C_1, C_2 and C_3 depend on the type of equipment. The pressure correction was applied only when the operating pressure fell within the corresponding validity range. When the pressure was below the lower limit of the correlation, F_P was set equal to unity.
In the present case, the pressure correction was applied to the evaporator, modeled as a fixed-tube-sheet heat exchanger, and to the centrifugal pump, for which the discharge pressure was considered. Conversely, the condenser operates close to atmospheric pressure and its pressure factor was therefore assumed equal to unity. The same assumption was adopted for the radial turbine, for which no pressure correction was required.
When the cost of a component was available for a reference size different from that required in the present plant, the six-tenths rule was used to account for the variation in equipment capacity.

According to this scaling relation, the purchase cost was estimated as:

$$\frac{C_{p,2}^0}{C_{p,1}^0} = \left(\frac{A_2}{A_1}\right)^{0.6} \tag{5.5}$$

where $C_{p,1}^0$ is the purchase cost associated with the reference size A_1, while $C_{p,2}^0$ is the estimated purchase cost for the required size A_2. The exponent 0.6 accounts for the economies of scale, since the equipment cost generally increases less than proportionally with its characteristic size.

Since the cost correlations refer to a specific reference year, the resulting values were updated to the year considered in the present analysis using the Chemical Engineering Plant Cost Index (CEPCI). The cost adjustment was performed according to:

$$\frac{C_1}{C_2} = \frac{I_1}{I_2} \tag{5.6}$$

where C_2 is the cost evaluated for the reference year associated with the original correlation, C_1 is the corresponding cost updated to the year considered in the present analysis, while I_2 and I_1 are the respective CEPCI values. Since the adopted correlations provide costs expressed in 2001 US dollars, a value of 397 was used for the 2001 index, while a value of 850 was adopted for 2026 [22].

Since the equipment costs obtained from the correlations are expressed in US dollars, they were converted into euros using the exchange rate recorded on 4 June 2026 [23]. On that date, the adopted exchange rate was:

$$1 \text{ EUR} = 1.164 \text{ USD} \tag{5.7}$$

Therefore, the conversion from US dollars to euros was performed according to:

$$C_{\text{EUR}} = \frac{C_{\text{USD}}}{1.164} \tag{5.8}$$

where C_{USD} is the cost expressed in US dollars and C_{EUR} is the corresponding value expressed in euros.
The heat transfer area of each heat exchanger was estimated using the logarithmic mean temperature difference method. The required area was calculated as:

$$A = \frac{\dot{Q}}{U \Delta T_{\text{lm}}} \tag{5.9}$$

where $\dot{Q}$ is the thermal duty of the heat exchanger, U is the overall heat transfer coefficient, and ΔT_{lm} is the logarithmic mean temperature difference between the hot and cold streams.

For a counter-current heat exchanger, the logarithmic mean temperature difference was evaluated as:

$$\Delta T_{\mathrm{lm}} = \frac{\Delta T_1 - \Delta T_2}{\ln\left(\frac{\Delta T_1}{\Delta T_2}\right)} \tag{5.10}$$

The overall heat transfer coefficients were selected on the basis of typical values reported in reference tables for tubular heat exchangers, taking into account the fluids involved and their phase-change conditions [24]. Conservative values were adopted to reflect the preliminary nature of the analysis and the absence of a detailed geometrical design of the heat exchangers.

The cost of the fluid inventory was estimated using a simplified rule-of-thumb approach. According to literature, its contribution to the overall plant cost is generally at least one order of magnitude lower than the cost of the main equipment [25]. Accordingly, the fluid costs were evaluated as a fraction of the equipment cost, adopting a more conservative assumption for Dowtherm-A than for toluene to account for their different commercial availability and expected market price.

The solar concentrator installed at the Energy Center was developed as a prototype and had an estimated purchase cost of approximately 18,000 €. However, this value is not considered representative of the unit cost of a solar field composed of several identical collectors, since only a very limited number of units were manufactured and the prototype price is likely to include non-recurring costs related to design, development and initial setup.

For this reason, the collector cost adopted in the present analysis was estimated from the cost correlations reported in the literature, which account for the effects of aperture area and production volume [26]. A specific cost of approximately 1,000€/m^2 was assumed. Considering a collecting area of 4.5 m^2, this corresponds to a unit cost of approximately 4,500€ per collector.

It should be noted that the collector cost includes only the additional units required for the plant. Although 23 and 20 collectors are needed for the base and regenerative configurations, respectively, one collector was excluded from the investment cost because it had already been purchased and is currently available at the Energy Center.

The cost of the alternator was estimated at approximately 200 €, representing only a minor contribution to the overall investment cost.

Despite the presence of the additional turbine and pump, the regenerative configuration results in a lower overall equipment cost. This reduction is mainly due to the smaller solar field required, which decreases the contribution of the solar collectors to the total investment.

	Base cycle	**Regenerative cycle**
Turbine 1	18,117 €	13,707 €
Turbine 2	/	9,222 €
Evaporator	29,033 €	28,238 €
Pump 1	2,309 €	497 €
Pump 2	/	2,179 €
Condenser	14,854 €	13,643 €
Solar collector	99,000 €	85,500 €
Alternator	200 €	200 €
Toluene	643 €	675 €
Dowtherm-A	3,216 €	3,374 €
TOTAL	**167,371 €**	**157,235 €**

Table 5.1: Contribution of each component to the total equipment cost

5.1.2 Estimation of EPCC

The EPCC was estimated from the BEC by including the additional costs associated with detailed engineering, procurement activities and construction management. According to the NETL methodology, these services can be estimated as (15-20%) of the BEC [20]. Given the limited size and relative simplicity of the plant considered in this study, the lower value of this range was adopted.

$$C_{\mathrm{EPCC}} = C_{\mathrm{BEC}}\,(1 + 0.15) \tag{5.11}$$

5.1.3 Estimation of TPC

The TPC was estimated by adding a project contingency to the EPCC. According to the NETL methodology, project contingency for preliminary cost estimates can be assumed in the range of 15–30%. In the present analysis, the lower value of 15% was adopted, since no separate process contingency was considered [20].

$$C_{\mathrm{TPC}} = C_{\mathrm{EPCC}}\,(1 + 0.15) \tag{5.12}$$

5.1.4 Estimation of TOC

The TOC was obtained by adding the owner's costs to the TPC. According to the NETL methodology, the following contributions were considered [20]:

- **Inventory capital:** 0.5% of the TPC, covering the initial stock of spare parts and consumable materials;
- **Pre-production costs:** 2% of the TPC, accounting for commissioning, operator training and initial maintenance requirements;
- **Financing costs:** 2.7% of the TPC, representing the expenses associated with securing project financing, excluding interest during construction;
- **Other owner's costs:** 15% of the TPC, including preliminary studies, permitting, legal expenses, owner's engineering and management reserve;
- **Land cost:** not included, since the plant is assumed to be installed within an existing facility of Politecnico di Torino and no additional land purchase is required;
- **Working capital:** not considered separately, in agreement with the assumptions adopted in the NETL methodology;
- **Technology royalties:** not included, since any related costs are assumed to be already included in the equipment purchase cost.

The TOC was consequently calculated as:

$$C_{\mathrm{TOC}} = C_{\mathrm{TPC}} \, (1 + 0.202) \tag{5.13}$$

5.1.5 Estimation of TASC

The TASC represents the overall capital expenditure incurred during the construction period. Unlike the TOC, it accounts for the cost of capital during construction. According to the NETL methodology, a factor of 1.093 is suggested for a three-year capital expenditure period [20]. This factor was adopted in the present analysis.

$$C_{\mathrm{TASC}} = C_{\mathrm{TOC}} \, (1.093) \tag{5.14}$$

The main capital cost levels obtained for the base and regenerative configurations are summarized in Table 5.2. The results show that the regenerative cycle leads to a lower cost at each stage of the estimation, mainly due to the reduced cost of the solar field.

	Base cycle	**Regenerative cycle**
BEC	167,371 €	157,235 €
EPCC	192,477 €	180,821 €
TPC	221,349 €	207,944 €
TOC	266,061 €	249,948 €
TASC	290,805 €	273,193 €

Table 5.2: Estimated capital costs for both configurations

5.2 Economic Performance Evaluation

The capital cost comparison presented in the previous section provides an estimate of the initial investment required for the base and regenerative configurations. However, the investment cost alone is not sufficient to assess their economic performance, since the two systems also differ in terms of electric power production and useful thermal energy available at the condenser.
For this reason, the economic comparison was carried out using the NPV method, which accounts for the time value of money by discounting the future cash flows generated during the operating life of the plant. For each configuration, the corresponding TASC was considered as the initial investment cost at year zero.
The NPV after N years is calculated as:

$$\mathrm{NPV}(t) = -I_0 + \sum_{n=1}^{t} \frac{CF_n}{(1+r)^n} \tag{5.15}$$

where I_0 is the initial investment cost, assumed equal to the TASC, CF_n is the net cash flow generated during year n, r is the discount rate and t is the number of operating years considered. The analysis was performed over an assumed plant lifetime of 20 years.

5.2.1 Discount Rate Estimation

Following the estimation of the initial investment cost, the economic performance of the two plant configurations was evaluated over the assumed operating lifetime. Since costs and revenues occurring in different years cannot be directly compared,

future cash flows must be discounted to their present value using an appropriate discount rate.
The economic analysis was performed at constant prices. Therefore, the future revenues and costs considered in the analysis are expressed in real terms, without including the effect of general price inflation. To maintain consistency between the cash flows and the discount rate, a real discount rate must consequently be adopted.
In the present analysis, the discount rate was determined starting from the nominal Weighted Average Cost of Capital (WACC), which represents the average cost of the financial resources used to support the investment. The nominal WACC was subsequently converted into a real discount rate by accounting for the expected inflation rate.
The WACC represents the average return required by the providers of capital and combines the cost of equity and the cost of debt according to their respective shares in the assumed financial structure of the investment.
The nominal WACC is calculated as:

$$\mathrm{WACC_n} = K_e \frac{E}{D+E} + K_d(1-\tau)\frac{D}{D+E} \tag{5.16}$$

where:

- K_e is the cost of equity;
- K_d is the pre-tax cost of debt;
- E is the market value of equity;
- D is the market value of debt;
- τ is the applicable corporate tax rate.

The factor $(1-\tau)$ generally accounts for the tax benefit associated with the deductibility of interest expenses. However, the present analysis considers the project within a public university facility and does not include corporate income taxation in the cash flows. Therefore, no tax benefit was attributed to debt financing, and τ was assumed equal to zero.

The cost of debt, K_d, was estimated as the sum of a reference interest rate and an additional financing spread:

$$K_d = \mathrm{IRS}_{5Y} + s \tag{5.17}$$

where IRS_{5Y} is the five-year interest rate swap adopted as the reference rate, while s is the additional spread applied by the lender to account for the financing risk.

In the present analysis, the five-year IRS was set equal to 2.76% [27], while the spread was assumed equal to 1%.

The cost of equity, K_e, was estimated using a Capital Asset Pricing Model (CAPM)-based approach. This method expresses the expected return required by equity investors as the sum of a risk-free rate and a risk premium related to the exposure of the investment to market risk. The general expression adopted is:

$$K_e = R_f + \beta \cdot \text{EMRP} + R_s \tag{5.18}$$

where:

- R_f is the risk-free rate;
- β is the coefficient that measures the sensitivity of the investment return to market variations;
- EMRP is the equity market risk premium, defined as the difference between the expected market return and the risk-free rate;
- R_s is an additional size or specific risk premium.

The equity market risk premium is therefore defined as:

$$\text{EMRP} = R_m - R_f \tag{5.19}$$

where R_m is the expected market return. In the present analysis, the risk-free rate R_f was assumed equal to 3.03%, based on the yield of Italian government bonds with a five-year maturity [28]. The equity market risk premium was set equal to 6% [29]. Since the project is not associated with a listed company, a specific market beta could not be directly derived from financial market data. Therefore, the coefficient β was assumed equal to 1, meaning that the systematic risk of the investment was considered comparable to the average market risk. The additional premium R_s was neglected, since the analysis does not refer to a small listed company or to a private equity investment characterized by reduced liquidity. Accordingly, R_s was assumed equal to zero.

Based on the assumptions described above, the cost of debt was estimated as $K_d = 3.76\%$, while the cost of equity resulted equal to $K_e = 9.03\%$. Considering an assumed capital structure composed of 60% equity and 40% debt, the resulting nominal WACC was:

$$\text{WACC}_\text{n} = 9.03\% \cdot 0.60 + 3.76\% \cdot 0.40 = 6.92\% \tag{5.20}$$

This value represents the nominal discount rate associated with the assumed financing structure. However, since the economic analysis is carried out at constant 2026 prices, the nominal WACC must be converted into a real discount rate before being used in the NPV calculation.
Since the economic analysis is performed at constant 2026 prices, the nominal WACC was converted into a real discount rate by removing the effect of expected inflation. The inflation rate was assumed equal to 2%, in line with the medium-term inflation target of the European Central Bank for the euro area [30].
The conversion was carried out using the Fisher equation, which relates the nominal discount rate, the real discount rate and the expected inflation rate:

$$1 + \mathrm{WACCn} = (1 + \mathrm{WACCr})\,(1 + \pi) \tag{5.21}$$

where WACCn is the nominal WACC, WACCr is the real WACC and π is the expected annual inflation rate. Rearranging Equation 5.21, the real WACC is obtained as:

$$\mathrm{WACCr} = \frac{1 + \mathrm{WACCn}}{1 + \pi} - 1 \tag{5.22}$$

Considering a nominal WACC equal to 6.92% and an expected inflation rate equal to 2%, the resulting real discount rate is:

$$\mathrm{WACC_r} = \frac{1 + 0.0692}{1 + 0.02} - 1 = 4.82\% \tag{5.23}$$

The resulting real WACC, equal to 4.82%, was therefore adopted as the discount rate for the subsequent NPV evaluation. This ensures consistency between the constant price cash flows and the discounting procedure used in the economic analysis.

5.2.2 Annual Savings and Incentives

Once the discount rate has been defined, the next step of the economic analysis consists in estimating the annual positive cash flows generated by the plant. In the present case, the system is assumed to operate mainly in a self-consumption configuration. Therefore, the economic benefit is not related to the direct sale of the produced energy, but rather to the avoided purchase of electricity from the grid and natural gas for thermal production.
The annual cash inflows were therefore evaluated by considering three contributions: the savings associated with the electricity produced by the ORC system, the savings related to the useful thermal energy recovered at the condenser, and the incentives potentially available for the improvement in energy efficiency.

The total annual cash inflow can be expressed as:

$$C_{\text{in,ann}} = S_{\text{el}} + S_{\text{th}} + I_{\text{ann}} \tag{5.24}$$

where S_{el} is the annual electricity saving, S_{th} is the annual thermal saving, and I_{ann} represents the annual incentive contribution.
The electricity saving was calculated by considering the net electric power produced by the plant, obtained as the difference between the electric power generated by the ORC system and the electric power consumed by the pump. This value was then multiplied by the annual operating hours and by the electricity purchase price for non-household consumers, obtained from Eurostat data [31]:

$$S_{\text{el}} = (W_{\text{el}} - W_{\text{pump}}) \cdot h_{\text{funz}} \cdot c_{\text{el}} \tag{5.25}$$

where W_{el} is the electric power produced by the ORC system, W_{pump} is the electric power required by the pump, h_{funz} is the annual operating time, and c_{el} is the electricity price.

Similarly, the useful thermal power recovered at the condenser was considered as a thermal output that can be used to satisfy an external heat demand. In the absence of the ORC plant, the same amount of useful heat would have to be supplied by a conventional natural gas boiler. Therefore, the thermal saving was evaluated as the avoided cost of producing this heat with the reference boiler.
The equivalent cost of useful thermal energy was calculated from the natural gas price for non-household consumers, obtained from Eurostat data [32], by taking into account the boiler efficiency:

$$c_{\text{th}} = \frac{c_{\text{gas}}}{\eta_{\text{boiler}}} \tag{5.26}$$

where c_{gas} is the natural gas price and η_{boiler} is the efficiency of the reference boiler. The annual thermal saving can then be expressed as:

$$S_{\text{th}} = Q_{\text{cond}} \cdot h_{\text{funz}} \cdot c_{\text{th}} \tag{5.27}$$

where Q_{cond} is the useful thermal power recovered at the condenser, h_{funz} is the annual operating time, and c_{th} is the equivalent cost of useful thermal energy.

The incentive contribution was evaluated by considering the Italian White Certificates mechanism, also known as Energy Efficiency Certificates.
This mechanism rewards energy efficiency improvements and can also be applied to high-efficiency cogeneration systems, where electricity and useful heat are produced simultaneously [33].

In the present study, the ORC plant was considered as a cogenerative system, since it produces net electric power and, at the same time, useful thermal power recovered at the condenser. Following the approach adopted for the estimation of the incentive [34], the annual primary energy saving was calculated as:

$$RISP = \frac{(W_{\text{el}} - W_{\text{pump}}) \cdot h_{\text{ann}}}{\eta_{\text{el,Italia}}} + \frac{Q_{\text{cond}} \cdot h_{\text{ann}}}{\eta_{\text{th,Italia}}} \tag{5.28}$$

where $\eta_{\text{el,Italia}}$ is the average efficiency of the Italian electricity system, assumed equal to 46%, while $\eta_{\text{th,Italia}}$ is the reference efficiency for thermal energy production, assumed equal to 90%.
The number of White Certificates associated with the annual primary energy saving was then obtained as:

$$CB = RISP \cdot 0.086 \cdot K \tag{5.29}$$

where 0.086 is the conversion factor from MWh to tonnes of oil equivalent, while K is a harmonization coefficient depending on the electric power of the unit. Since the plant analysed in this work has an electric power lower than 1 MW, K was assumed equal to 1.4 [35].
Finally, the annual incentive contribution was calculated by multiplying the number of White Certificates by their unit value:

$$I_{\text{ann}} = CB \cdot p_{\text{CB}} \tag{5.30}$$

where p_{CB} is the assumed economic value of one White Certificate. Since one White Certificate, or Energy Efficiency Certificate, corresponds to one tonne of oil equivalent saved, the unit value can be expressed in €/CB or, equivalently, in €/toe. In this work, a unit value of 260 €/CB was considered, corresponding to 260 €/toe, in agreement with the value reported for White Certificates [36].

According to the regulation, for units entering into operation after new construction or refurbishment after 6 March 2007 and connected to a district heating network, the incentive is granted for 15 calendar years starting from 1 January of the year following the commissioning date [33]. For this reason, the White Certificates contribution was included in the cash-flow analysis for the first 15 years of plant operation.

The annual savings and the economic contribution associated with the White Certificates mechanism are summarized in Table 5.3. The total annual cash inflow was obtained as the sum of the annual savings, indicated as R_{ann}, and the annual incentive contribution, indicated as I_{CB}.

Configuration	Annual savings	White Certificates incentive
Base case	23,118 €/year	8,529 €/year
Regenerative	20,552 €/year	7,564 €/year

Table 5.3: Annual savings and incentives

As expected, the base case configuration leads to higher annual cash inflows, mainly because of the larger amount of useful thermal energy recovered at the condenser. In the regenerative configuration, the internal heat recovery reduces the condenser heat duty and, consequently, both the thermal savings and the incentive contribution are lower.

5.2.3 Net Present Value Results

The cash-flow analysis for the base case configuration is reported in Table 5.4. The annual OPEX was estimated as 1% of the TASC, while the revenues include both the annual savings and the White Certificates contribution during the first 15 years. From year 16 onward, only the annual savings were considered, since the incentive period is no longer active. The net cash flow, indicated as B, was obtained by subtracting the annual OPEX from the corresponding revenues.

Base case scenario					
Year	**OPEX**	**Revenues**	B	**Discount factor**	**NPV**
0	0	0	-290,805 €	1.00	-290,805 €
1	-2,908 €	31,648 €	28,739 €	1.05	-263,388 €
2	-2,908 €	31,648 €	28,739 €	1.10	-237,234 €
3	-2,908 €	31,648 €	28,739 €	1.15	-212,283 €
4	-2,908 €	31,648 €	28,739 €	1.21	-188,481 €
5	-2,908 €	31,648 €	28,739 €	1.27	-165,775 €
6	-2,908 €	31,648 €	28,739 €	1.33	-144,114 €
7	-2,908 €	31,648 €	28,739 €	1.39	-123,450 €
8	-2,908 €	31,648 €	28,739 €	1.46	-103,738 €
9	-2,908 €	31,648 €	28,739 €	1.53	-84,933 €
10	-2,908 €	31,648 €	28,739 €	1.60	-66,993 €
11	-2,908 €	31,648 €	28,739 €	1.68	-49,880 €
12	-2,908 €	31,648 €	28,739 €	1.76	-33,554 €
13	-2,908 €	31,648 €	28,739 €	1.85	-17,979 €
14	-2,908 €	31,648 €	28,739 €	1.93	-3,122 €
15	-2,908 €	31,648 €	28,739 €	2.03	11,051 €
16	-2,908 €	23,118 €	20,210 €	2.13	20,560 €
17	-2,908 €	23,118 €	20,210 €	2.23	29,630 €
18	-2,908 €	23,118 €	20,210 €	2.34	38,283 €
19	-2,908 €	23,118 €	20,210 €	2.45	46,538 €
20	-2,908 €	23,118 €	20,210 €	2.57	54,413 €

Table 5.4: Cash-flow analysis for the base case scenario

The evolution of the cumulative discounted cash flow for the base case scenario is shown in Figure 5.1. The curve highlights the progressive recovery of the initial investment and shows that the NPV becomes positive during the fifteenth year of operation.

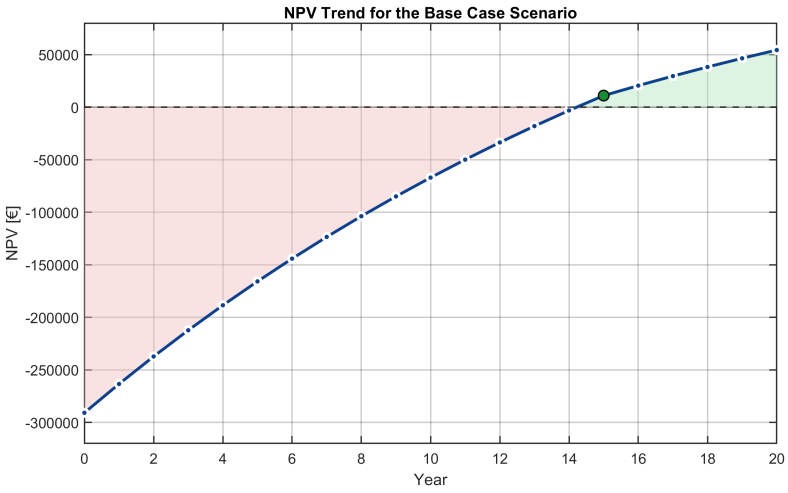


Figure 5.1: NPV trend for the base case scenario

The yearly cash-flow values obtained for the regenerative configuration are reported in Table 5.5.

Regenerative case scenario					
Year	**OPEX**	**Revenues**	B	**Discount factor**	**NPV**
0	0	0	-273,193 €	1.00	-273,193 €
1	-2,732 €	28,115 €	25,383 €	1.05	-248,979 €
2	-2,732 €	28,115 €	25,383 €	1.10	-225,879 €
3	-2,732 €	28,115 €	25,383 €	1.15	-203,842 €
4	-2,732 €	28,115 €	25,383 €	1.21	-182,820 €
5	-2,732 €	28,115 €	25,383 €	1.27	-162,766 €
6	-2,732 €	28,115 €	25,383 €	1.33	-143,634 €
7	-2,732 €	28,115 €	25,383 €	1.39	-125,384 €
8	-2,732 €	28,115 €	25,383 €	1.46	-107,973 €
9	-2,732 €	28,115 €	25,383 €	1.53	-91,365 €
10	-2,732 €	28,115 €	25,383 €	1.60	-75,520 €
11	-2,732 €	28,115 €	25,383 €	1.68	-60,405 €
12	-2,732 €	28,115 €	25,383 €	1.76	-45,986 €
13	-2,732 €	28,115 €	25,383 €	1.85	-32,230 €
14	-2,732 €	28,115 €	25,383 €	1.93	-19,108 €
15	-2,732 €	28,115 €	25,383 €	2.03	-6,590 €
16	-2,732 €	20,552 €	17,820 €	2.13	1,794 €
17	-2,732 €	20,552 €	17,820 €	2.23	9,791 €
18	-2,732 €	20,552 €	17,820 €	2.34	17,421 €
19	-2,732 €	20,552 €	17,820 €	2.45	24,699 €
20	-2,732 €	20,552 €	17,820 €	2.57	31,642 €

Table 5.5: Cash-flow analysis for the regenerative case scenario

For the regenerative configuration, the cumulative discounted cash flow becomes positive during the sixteenth year of operation.
The corresponding NPV trend is shown in Figure 5.2.

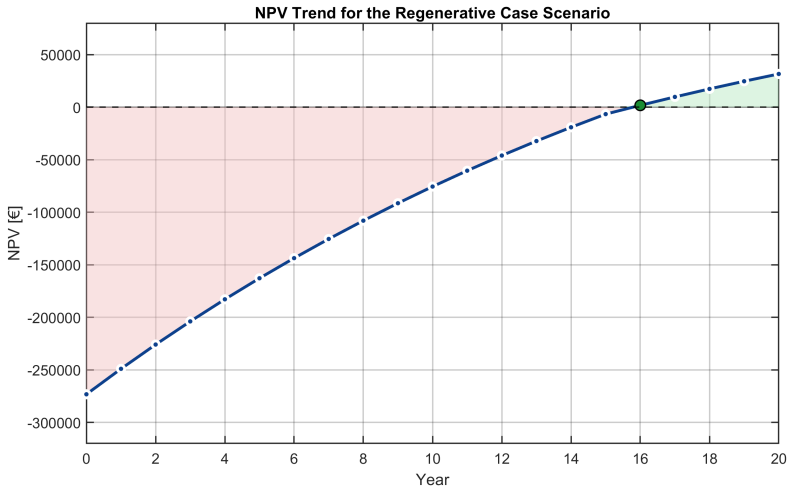


Figure 5.2: NPV trend for the regenerative case scenario

The comparison between the two configurations shows that the base case scenario provides the best economic performance. Although it requires a higher initial investment, the larger annual cash inflows allow the investment to be recovered earlier and lead to a higher final NPV. For this reason, the base case configuration was selected as the most convenient solution from an economic point of view.

Since the base case scenario showed the best economic performance, additional economic indicators were evaluated only for this configuration:

- **Internal Rate of Return (IRR):** it represents the discount rate that makes the NPV equal to zero. It is used to assess the profitability of the investment and to compare it with the discount rate adopted in the analysis.
- **Levelized Cost of Electricity (LCOE):** it represents the selling price of electricity required to recover the investment and operating costs of the plant. In this indicator, the plant is assumed to produce only electric energy.
- **Levelized Cost of Heat (LCOH):** it represents the selling price of the useful thermal energy required to recover the investment and operating costs of the plant. In this case, the plant is assumed to produce only thermal energy.
- **Levelized Cost of Energy (LCOE′):** it is a modified levelized cost indicator introduced to account for the cogenerative nature of the system. Both the

electric energy produced by the ORC system and the useful thermal energy recovered at the condenser are considered as useful outputs, assuming the same unit value for the overall energy production.

The values obtained for the base case scenario are reported in Table 5.6.

IRR	**LCOE**	**LCOH**	**LCOE′**
7.05%	0.765 €/kWhel	0.145 €/kWhth	0.122 €/kWh

Table 5.6: Additional economic indicators for the base case scenario

The Internal Rate of Return, equal to 7.05%, is higher than the real discount rate adopted in the analysis, confirming the economic feasibility of the selected configuration under the assumptions considered. The relatively high value of the Levelized Cost of Electricity is mainly due to the small electric power output of the plant. On the other hand, the lower values of the Levelized Cost of Heat and LCOE′ highlight the important contribution of the useful thermal energy recovered at the condenser, which improves the overall economic performance of the cogenerative system.

Overall, the economic analysis confirms that the base case configuration represents the most convenient solution among the two toluene-based layouts considered. Although the regenerative configuration requires a lower initial investment due to the smaller solar field, this advantage is not sufficient to compensate for the lower annual cash inflows associated with the reduced electric output and useful heat recovery. Under the assumptions adopted in this preliminary assessment, the base case scenario achieves a higher final NPV, an earlier investment recovery and a positive IRR with respect to the real discount rate. Therefore, the base toluene configuration is selected as the reference solution for the final assessment of the plant.

Chapter 6

Conclusions

This thesis investigated the modeling and techno-economic assessment of a small-scale Organic Rankine Cycle coupled with parabolic dish collectors for cogenerative applications. The main objective was to evaluate the performance of different working fluids and cycle configurations, and to identify the most suitable solution for a solar-driven system designed to produce both electric power and useful heat.

The first part of the work provided an overview of the main CSP technologies, with particular attention to parabolic dish collectors. Compared with other CSP configurations, parabolic dishes are characterized by high optical efficiency, high concentration ratios and a modular structure. These features make them particularly suitable for small-scale applications, such as the system considered in this work.

The ORC system was modeled in Aspen Plus under steady-state conditions using the Peng–Robinson equation of state. Three working fluids were analyzed: MDM, toluene and D4. The main components of the cycle, namely turbine, condenser, pump and evaporator, were first modeled separately through sensitivity analyses. The same nominal turbine mechanical power output of 10 kW was imposed for all fluids, in order to compare their behavior under consistent operating conditions.
A regenerative ORC layout was then investigated for all the selected fluids. The regenerative configuration reduces the external thermal power required by the evaporator by using an intermediate extraction of the working fluid to preheat the stream before the evaporator. This leads to higher electric and ORC efficiency values and to a lower number of required collectors. However, the regenerative layout also reduces the total turbine power output and the useful heat recovered at the condenser. Therefore, the improvement in efficiency does not automatically lead to a better overall economic performance.
The results showed that toluene provides the most favorable compromise among

the selected working fluids. For this reason, toluene was selected as the reference working fluid for the following economic assessment.

The solar field was sized using the evaporator thermal demand as reference. Based on the estimated annual average DNI and the optical efficiency of the collector, a single parabolic dish was found to provide approximately 2.71 kW_{th} of useful thermal power. For the toluene case, the base configuration requires 23 collectors, while the regenerative configuration requires 20 collectors. Although regeneration reduces the size of the solar field, the base configuration provides higher useful energy production.

The economic assessment was performed by estimating the capital cost levels from BEC to TASC and by evaluating the Net Present Value over a 20-year plant lifetime. The base configuration has a higher initial investment, with a TASC of 290,805 €, compared with 273,193 € for the regenerative configuration. Nevertheless, the base case generates higher annual cash inflows due to the larger electric and thermal energy production. As a result, the base configuration reaches a positive NPV during the fifteenth year of operation and achieves a final NPV of 54,413 €. The regenerative configuration becomes positive during the sixteenth year and reaches a final NPV of 31,642 €.

In conclusion, under the assumptions adopted in this work, the most suitable configuration is the base ORC cycle operating with toluene. This solution offers the best compromise between thermodynamic performance, solar field size and economic return. The regenerative configuration remains interesting from an energy-efficiency point of view, but its lower electric output and reduced heat recovery make it less convenient in the economic scenario considered.

Future developments could include a more detailed design of the solar receiver and heat exchangers, the introduction of transient simulations based on real solar irradiance profiles, and the integration of a thermal energy storage system to extend the operating time of the plant. A more detailed economic analysis could also be carried out by considering updated commercial quotations, different incentive schemes and sensitivity analyses on electricity price, natural gas price, discount rate and investment cost. Finally, experimental validation of the ORC system and of the solar receiver would be necessary to confirm the assumptions adopted in the numerical model.

Bibliography

[1] IEA. *Electricity 2026*. Tech. rep. Licence: CC BY 4.0. Paris: International Energy Agency, 2026. URL: https://www.iea.org/reports/electricity-2026 (cit. on p. 1).

[2] Abdul Hai Alami, AG Olabi, Ayman Mdallal, Ahmed Rezk, Ali Radwan, Shek Mohammod Atiqure Rahman, Sheikh Khaleduzzaman Shah, and Mohammad Ali Abdelkareem. «Concentrating solar power (CSP) technologies: Status and analysis». In: *International Journal of Thermofluids* 18 (2023), p. 100340 (cit. on p. 2).

[3] Maria Simona Răboacă, Gheorghe Badea, Adrian Enache, Constantin Filote, Gabriel Răsoi, Mihai Rata, Alexandru Lavric, and Raluca-Andreea Felseghi. «Concentrating Solar Power Technologies». In: *Energies* 12.6 (2019). ISSN: 1996-1073. DOI: 10.3390/en12061048. URL: https://www.mdpi.com/1996-1073/12/6/1048 (cit. on p. 2).

[4] Patricia Scalco, Jacqueline Biancon Copetti, Mario Henrique Macagnan, and Jeferson Diehl de Oliveira. «Linear fresnel solar collector concentrator–a review». In: (2021) (cit. on pp. 3, 7).

[5] VK Jebasingh and GM Joselin Herbert. «A review of solar parabolic trough collector». In: *Renewable and Sustainable Energy Reviews* 54 (2016), pp. 1085–1091 (cit. on pp. 4, 7).

[6] Kolli Harish Kumar, Ahmed M Daabo, Malay K Karmakar, and Harish Hirani. «Solar parabolic dish collector for concentrated solar thermal systems: a review and recommendations». In: *Environmental Science and Pollution Research* 29.22 (2022), pp. 32335–32367 (cit. on pp. 5, 7).

[7] Chao Xu, Zhifeng Wang, Xin Li, and Feihu Sun. «Energy and exergy analysis of solar power tower plants». In: *Applied thermal engineering* 31.17-18 (2011), pp. 3904–3913 (cit. on pp. 6, 7).

[8] Muhammad Kamran and Muhammad Rayyan Fazal. *Renewable energy conversion systems*. Academic Press, 2021 (cit. on p. 6).

[9] Mohammed Alhwayzee, Hayder Jawad Kadhim, and Farhan Lafta Rashid. «Aspen Plus Simulation for Performance Improving of Al-Khayrat Power Plant Using Heat Recovery Steam Generation (HRSG) System». In: *Journal of Mechanical Engineering Research and Developments* 44.4 (2021), pp. 400–411 (cit. on pp. 9, 10).

[10] Jos'e C. Jim'enez-Garc'ia, Alexis Ruiz, Alejandro Pacheco-Reyes, and Wilfrido Rivera. «A Comprehensive Review of Organic Rankine Cycles». In: *Processes* 11.7 (2023), p. 1982. DOI: 10.3390/pr11071982. URL: https://www.mdpi.com/2227-9717/11/7/1982 (cit. on pp. 11, 12, 14, 43).

[11] Kankeyan Thurairaja, Anusha Wijewardane, Saliya Jayasekara, and Chathura Ranasinghe. «Working fluid selection and performance evaluation of ORC». In: *Energy Procedia* 156 (2019), pp. 244–248 (cit. on p. 13).

[12] Junjiang Bao and Li Zhao. «A review of working fluid and expander selections for organic Rankine cycle». In: *Renewable and sustainable energy reviews* 24 (2013), pp. 325–342 (cit. on pp. 14, 15).

[13] Huijuan Chen, D Yogi Goswami, and Elias K Stefanakos. «A review of thermodynamic cycles and working fluids for the conversion of low-grade heat». In: *Renewable and sustainable energy reviews* 14.9 (2010), pp. 3059–3067 (cit. on pp. 15–17).

[14] Mohammad Shalby, Abdullah Marachli, and Ahmad A Salah. «Working fluid selection and performance analysis for subcritical organic Rankine cycles». In: *Results in Engineering* 25 (2025), p. 104120 (cit. on pp. 16, 19–21).

[15] CoolProp. *MDM – Octamethyltrisiloxane*. https://coolprop.org/fluid_properties/fluids/MDM.html. Accessed: 10 April 2026. 2026 (cit. on p. 19).

[16] CoolProp. *Toluene*. https://coolprop.org/fluid_properties/fluids/Toluene.html. Accessed: 10 April 2026. 2026 (cit. on p. 19).

[17] CoolProp. *D4 – Octamethylcyclotetrasiloxane*. https://coolprop.org/fluid_properties/fluids/D4.html. Accessed: 10 April 2026. 2026 (cit. on p. 20).

[18] Dow. *DOWTHERM A Heat Transfer Fluid*. 2026. URL: https://www.dow.com/en-us/pdp.dowtherm-a-heat-transfer-fluid.238000z.html?productCatalogFlag=1 (cit. on p. 21).

[19] Leonardo Ricci and Davide Papurello. «A Prediction Model for Energy Production in a Solar Concentrator Using Artificial Neural Networks». In: *International Journal of Energy Research* 2023 (2023), pp. 1–20. DOI: 10.1155/2023/9196506. URL: https://doi.org/10.1155/2023/9196506 (cit. on p. 22).

[20] Joel Theis. *Quality Guidelines for Energy System Studies: Cost Estimation Methodology for NETL Assessments of Power Plant Performance*. Tech. rep. NETL-PUB-22580. National Energy Technology Laboratory (NETL), Feb. 2021. DOI: 10.2172/1567736. URL: https://netl.doe.gov/projects/files/QGESSCostEstMethodforNETLAssessmentsofPowerPlantPerformance_022621.pdf (cit. on pp. 62, 67, 68).

[21] Richard Turton, Richard C. Bailie, Wallace B. Whiting, and Joseph A. Shaeiwitz. *Analysis, Synthesis, and Design of Chemical Processes*. 3rd ed. Upper Saddle River, NJ: Prentice Hall, 2009. ISBN: 9780135129661 (cit. on p. 63).

[22] Chemical Engineering. *Plant Cost Index Beta*. Accessed: 4 June 2026. 2026 (cit. on p. 65).

[23] European Central Bank. *Euro Foreign Exchange Reference Rates: US Dollar*. Exchange rate accessed on 4 June 2026. 2026 (cit. on p. 65).

[24] Don W. Green and Robert H. Perry, eds. *Perry's Chemical Engineers' Handbook*. 8th ed. McGraw-Hill, 2008. ISBN: 9780071422949 (cit. on p. 66).

[25] Marco Astolfi, Matteo C Romano, Paola Bombarda, and Ennio Macchi. «Binary ORC (Organic Rankine Cycles) power plants for the exploitation of medium–low temperature geothermal sources–Part B: Techno-economic optimization». In: *Energy* 66 (2014), pp. 435–446 (cit. on p. 66).

[26] Giacomo Gavagnin, David S'anchez, Gonzalo S. Mart'inez, Jos'e M. Rodr'iguez, and Antonio Mu noz. «Cost analysis of solar thermal power generators based on parabolic dish and micro gas turbine: Manufacturing, transportation and installation». In: *Applied Energy* 194 (2017), pp. 108–122. DOI: 10.1016/j.apenergy.2017.02.052 (cit. on p. 66).

[27] MutuiOnline S.p.A. *Guide mutuo: guide e strumenti per il mutuo*. https://mutuionline.24oreborsaonline.ilsole24ore.com/guide-mutui/. 24 Ore Mutui Online. 2026 (cit. on p. 71).

[28] Ministero dell'Economia e delle Finanze – Dipartimento del Tesoro. *Dati statistici sul debito pubblico*. https://www.dt.mef.gov.it/it/debito_pubblico/dati_statistici/. 2026 (cit. on p. 71).

[29] Statista. *Average market risk premium by country in Europe 2025*. https://www.statista.com/statistics/664786/average-market-risk-premium-selected-countries-europe/. Published: 3 March 2026. 2026 (cit. on p. 71).

[30] European Central Bank. *Price stability and the two per cent inflation target*. 2026. URL: https://www.ecb.europa.eu/mopo/strategy/pricestab/html/index.en.html (cit. on p. 72).

[31] Eurostat. *Electricity prices for non-household consumers - bi-annual data (from 2007 onwards)*. 2026. DOI: 10.2908/nrg_pc_205. URL: https://ec.europa.eu/eurostat/databrowser/view/nrg_pc_205/default/table?lang=en (cit. on p. 73).

[32] Eurostat. *Gas prices for non-household consumers - bi-annual data (from 2007 onwards)*. 2026. DOI: 10.2908/nrg_pc_203. URL: https://ec.europa.eu/eurostat/databrowser/view/nrg_pc_203/default/table?lang=en (cit. on p. 73).

[33] Gestore dei Servizi Energetici. *Certificati Bianchi*. GSE – Efficienza energetica. 2026. URL: https://www.gse.it/servizi-per-te/efficienza-energetica/certificati-bianchi (cit. on pp. 73, 74).

[34] Gestore dei Servizi Energetici. *Guida alla Cogenerazione ad Alto Rendimento – Aggiornamento 2019*. GSE – Cogenerazione ad Alto Rendimento. 2019. URL: https://www.gse.it/documenti_site/Documenti%20GSE/Servizi%20per%20te/COGENERAZIONE%20AD%20ALTO%20RENDIMENTO/Guide/Aggiornamento%20Guida%20CAR%20-%20revisione%202019.pdf (cit. on p. 74).

[35] Ministero dello Sviluppo Economico. *D.M. 5 settembre 2011: Definizione del nuovo regime di sostegno per la cogenerazione ad alto rendimento*. Pubblicato nella Gazzetta Ufficiale n. 218 del 19 settembre 2011. 2011. URL: https://www.fire-italia.org/prova/wp-content/uploads/2014/03/DM-5_09_2011.pdf (cit. on p. 74).

[36] RiESCo S.p.A. *Quanto valgono i Certificati Bianchi?* Valore economico dei Certificati Bianchi o Titoli di Efficienza Energetica. 2020. URL: https://www.ri-esco.it/certificati-bianchi-valore/ (cit. on p. 74).